DOI:10.14753/SE.2015.1797

Non-invasive Characterization of Coronary Artery Atherosclerotic Plaques

Doctoral Dissertation

Mihály Károlyi

Doctoral School of Basic Medical Sciences
Semmelweis University

Supervisors: Dr. Pál Maurovich-Horvat Ph.D.
Dr. Béla Merkely D.Sc.

Official reviewers: Dr. Lívia Jánoskúti Ph.D.
Dr. Attila Thury Ph.D.

Head of the Final Examination Committee:
Dr. Viktor Bérczi D.Sc.

Members of the Final Examination Committee:
Dr. Attila Doros Ph.D.
Dr. László Sallai Ph.D.

Budapest, 2015

DOI:10.14753/SE.2015.1797

Table of Contents

DOI:10.14753/SE.2015.1797

DOI:10.14753/SE.2015.1797

Abbreviations

3D	3 Dimensional
ACS	Acute Coronary Syndrome
AHA	American Heart Association
ASIR	Adaptive Statistical Iterative Reconstruction
CA	Lipid-Rich Necrotic Core Area
CABG	Coronary Artery Bypass Grafting
CAD	Coronary Artery Disease
CI	Confidence Interval
CNR	Contrast-to-Noise Ratio
CT	Computed Tomography
CTA	Computed Tomography Angiography
FBPR	Filtered Backprojection Reconstruction
FOV	Field of View
HU	Hounsfield Unit
ICC	Intraclass Correlation Coefficient
IIAM	International Institute for the Advancement of Medicine
IQ	Image Quality
IVUS	Intravascular Ultrasound
kV	Kilovolt
LA	Luminal Area
LAD	Left Anterior Descending Coronary Artery
LCX	Left Circumflex Coronary Artery
LRNC	Lipid-Rich Necrotic Core
mAs	Milliampere-second
MBIR	Model-Based Iterative Reconstruction
mmHg	Millimeter of Mercury
MRI	Magnetic Resonance Imaging
NcA	Non-core Plaque Area
NRS	Napkin-Ring Sign
OCT	Optical Coherence Tomography
PB	Plaque Burden
PCI	Percutaneous Coronary Intervention
RCA	Right Coronary Artery
RF	Radiofrequency
ROI	Regions of Interest
T	Tesla
TCFA	Thin-Cap Fibroatheroma
TE	Time of Echo
TPA	Total Plaque Area
TR	Time of Repetition
UTE	Ultra-Short Echo Time
VA	Vessel Area

DOI:10.14753/SE.2015.1797

1. Introduction

Coronary atherosclerosis related cardiac events remain the leading cause of morbidity and mortality worldwide (1). Most acute coronary events can be linked to the rupture of a coronary atherosclerotic plaque, resulting in the formation of a luminal thrombus and possible occlusion of the vessel (2). Similar atherosclerotic lesions are also present in individuals who did not experience acute cardiovascular event (3). Autopsy studies have revealed features specific to plaques vulnerable to rupture such as increased plaque dimensions, a large lipid-rich necrotic core and a thin fibrotic cap separating the necrotic core from the vessel lumen (4-6). To date invasive techniques such as intravascular ultrasound (IVUS) and optical coherence tomography (OCT) are the clinical gold standards to study plaque morphology associated with acute coronary events (7,8). IVUS permits not only invasive imaging of the entire arterial wall with high spatial and temporal resolution, discriminating plaque components, but both accurate and highly reproducible detection and cross-sectional quantification of coronary atherosclerotic plaque burden (9,10). OCT is an optical analogue of IVUS allowing for high-resolution tomographic intra-arterial visualization of the coronaries and it has also been validated for characterizing various plaque components as compared to histology (11). However, these techniques are not appropriate for large-scale screening or serial follow-up studies. Thus, significant interest exists in the development of non-invasive imaging techniques to characterize atherosclerotic lesions, assess their risk for rupture and further complications. Furthermore, over-time change in atherosclerotic plaque burden represents a potential surrogate endpoint indicating the efficacy of novel anti-atherosclerotic drugs, underlining the potential of non-invasive techniques in follow-up of patient treatment (9).

DOI:10.14753/SE.2015.1797

1.1 Natural history of atherosclerosis and concept of the vulnerable plaque

Atherosclerosis is as a chronic inflammatory disease that incubates over decades and affects the global arterial vasculature. Complex interactions between cellular factors and molecular messengers both in the vessel wall and blood are required for its evolution. Vascular injury and endothelial dysfunction are considered as the triggers for atherosclerotic inflammatory cell activation. Their appearance promotes the infiltration, accumulation and modification of lipoproteins in the vessel wall. The various combinations of these lipoproteins with extracellular matrix components (collagen, proteoglycans), smooth muscle cells, inflammatory cells (macrophages, T lymphocytes), calcium and new blood vessels (angiogenesis) results in the buildup of an atherosclerotic plaque (12).

The conversion of chronic atherosclerotic lesions to complicated thrombotic plaques happens often suddenly without any prior warning symptoms of the patient. Therefore the mechanisms leading to such complications have been studied extensively in the past years. Early investigations hypothesized, that ST-segment elevation acute coronary syndrome (ACS) results from a progressive, high-grade luminal narrowing of the coronary artery, which is complicated by a small platelet thrombi occluding the vessel completely and arresting myocardial blood supply. Accordingly, myocardial infarction with no ST-segment elevation would result from a transient or incomplete occlusion of a critical lesion in the culprit coronary artery. Current diagnostic approaches of atherosclerotic lesions are generally based on these concepts. Invasive catheterization visualizes the arterial luminal narrowing directly, while other diagnostic techniques (e.g., stress tests, perfusion imaging) evaluate ischemia related to fixed stenotic lesions. Treatment strategies as percutaneous coronary intervention (PCI) and coronary artery bypass grafting (CABG) also target these stenotic lesions (12).

Recent clinical and pathological observations have challenged these commonly ingrown notions (12-15). According to serial angiographic studies, plaques at the site of the culprit lesion deemed responsible for future myocardial infarction usually do not cause flow-limiting stenosis. The Prospective Natural-History Study of Coronary

Atherosclerosis (PROSPECT) investigated and followed-up for 3 years near 700 patients who underwent three-vessel coronary angiography and IVUS imaging after percutaneous coronary intervention due to ACS. Surprisingly, only about 50% of subsequent events arose from stenotic plaques that might have warranted interventionists at the time of PCI (16). Also, angiographic control after thrombolytic therapy of the occluding thrombus often reveals a non-stenotic underlying lesion in the artery. Recent studies with computed tomography imaging, which allows the visualization of the arterial wall beyond luminal narrowing, have particularly evaluated the characteristics of such lesions. Outward expansion of the arterial wall (positive remodeling) and plaque with little of no calcification has been associated with ACS (17,18). These lesions also lie usually proximal to the location of the maximal luminal stenosis, which is the target of conventional revascularization therapies (19). These observations explain the fact that myocardial infarction or sudden cardiac death is often the first sign of coronary atherosclerosis, while culprit lesions stay hidden and do not cause prior angina pectoris for the patient. In line with these observations the Clinical Utilizing Revascularization and Aggressive Drug Evaluation (COURAGE) trial found that medical therapy is equally preventive for future acute coronary events as invasive revascularization procedures (20). This assembly of clinical findings turned researchers attention to the early identification of silent lesions at increased risk of acute coronary events and proposed the concept of the vulnerable (21).

The term vulnerable or high-risk plaque is generally accepted for lesions at increased risk of thrombosis (or recurrent thrombosis) and rapid stenosis progression (22). Autopsy studies were extensively performed to reveal the specific characteristics of such lesions (5,13,15). Their findings underscored the clinical observation, that luminal narrowing occurs relatively late in the atherogenesis process, when plaque evolution outstrips the capability of the artery for compensatory expansion (23). This results in a substantial burden of atheromatosus plaque outward the lumen preventing stenosis and obscuring the clinical signs of ischemia for the patient (12).

Different forms of atherosclerotic lesions are presented in **Figure 1**. Histopathological features of an advance atherosclerotic plaque (thin-cap fibroatheroma) are shown in **Figure 2**, while **Figure 3** summarizes the stages of plaque evolution.

DOI:10.14753/SE.2015.1797

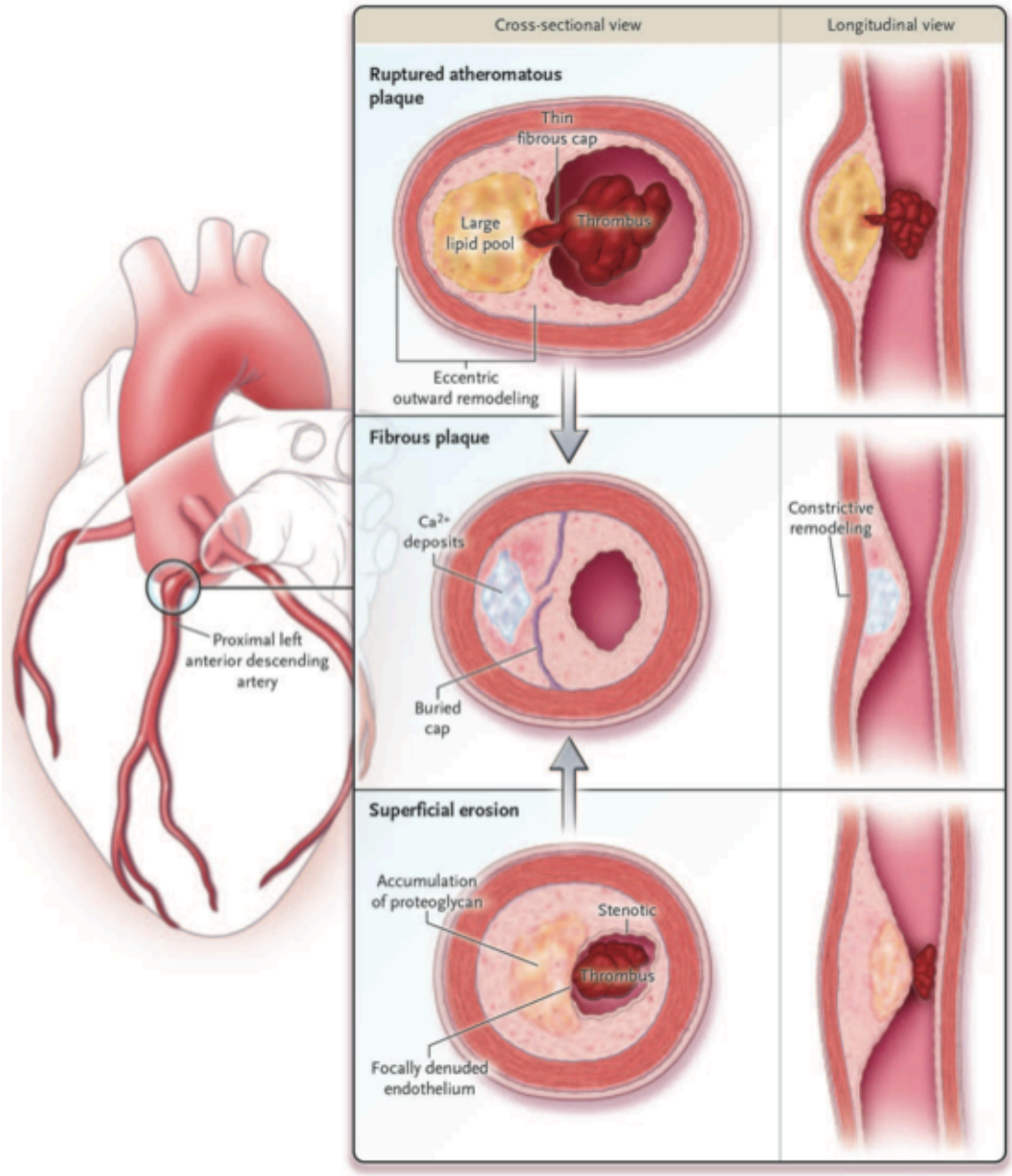

Figure 1 – Different presentations of coronary atherosclerosis.

Cross-sectional images of plaques at the proximal left anterior descending artery. *Upper* image represents a positively remodelled excentric fibroatheroma with thrombus formation provoken by the fibrous cap rupture. *Middle* image shows the healed plaque rupture resulting in a more fibrous lesion. Strata represents the buried fibrous cap from prior disruption. Progressive fibrosis and calcification may be present. These lesions narrow the lumen and may cause stable ischemic symptomes to the patient. *Bottom* image represents a proteoglycan rich plaque eroded at the intimal surface, causing occlusive thrombus (12). Typically three types of atherosclerotic plaque morphologies are associated with acute coronary syndromes: plaque rupture, plaque erosion and calcified nodule (12,13). The rupture of a thin, inflamed cap covering a lipid-rich, necrotic center of a plaque, termed as “thin-cap fibroatheromas” (TCFA) is responsible for the majority of fatal coronary events. The fibrous cap separates the

thrombogenic material enriched in the lipid core and the latent coagulant factors of the blood compartment (12). Fibrous cap thickness under 50-65 μm was identified as the cut-off indicating plaques causing fatal ruptures (13,24,25).

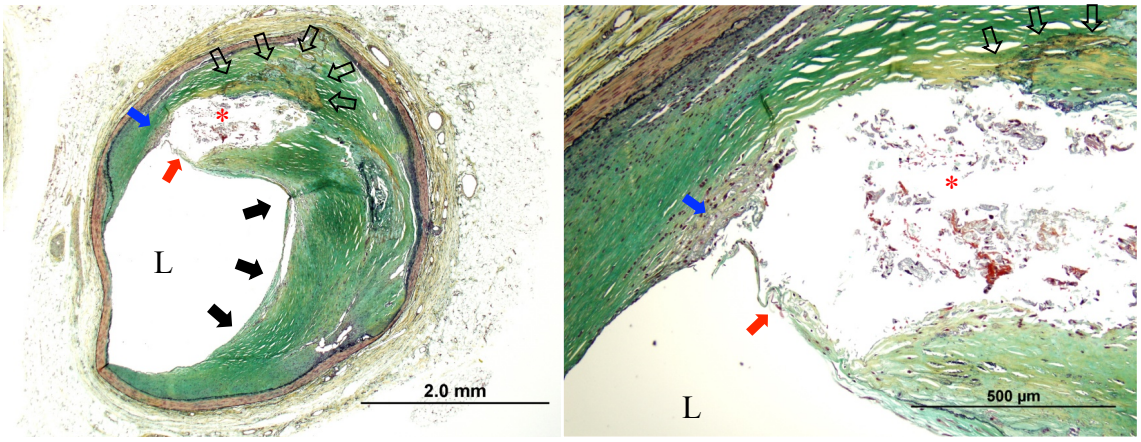

Figure 2 – Histopathological images of a thin-cap fibroatheroma.

The intact fibroatheroma plaque was reveled in a 61-year-old male, who died suddenly in ischemic stroke and had a history of coronary artery disease. The plaque was located in the proximal left anterior descending coronary artery and resulted in 50% cross-sectional luminal narrowing. Note the large necrotic core (*) seperated with a thin fibrous cap (red arrow) from the vessel lumen (L). The core is surrounded with prominent fibrotic tissue (closed arrows) and a sheet calcification (open arrows). Additional machrophage infiltration (blue arrow) is present within the plaque (unpublished data).

Thrombosis-prone plaques are also generally larger, have significant size of lipid-rich necrotic cores and show punctuate or spotty calcification (18,26). Abundant inflammatory cell accumulation was also discovered as characteristic for high-risk lesions. Macrophages and their mediators (matrix-metalloproteinase enzymes) are hold responsible for the disruption of collagen, which stabilizes the fibrous cap and prevents plaque rupture (12,27,28). The superficial erosion of atheromatosus plaques triggers 20-25% of fatal acute coronary syndromes (13). Endothelial cell desquamation due to programmed cell death, oxidative stress and hypochlorous acid initiated apoptosis associated with inflammatory cells could contribute to plaque erosion (29,30). Intimal erosion of a calcified nodule protruding into the lumen and intraplaque hemorrhage may be responsible for only a small proportion of acute coronary syndromes (13).

Importantly, compelling evidence suggest that plaque rupture and thrombus formation are frequent events that are instrumental in plaque evolution and luminal stenosis

development (13,31). Thus, a ruptured atherosclerotic plaque and a formatted thrombus typically do not cause coronary events (13,21). Numerous healed plaque ruptures are essential for the development of a high-grade luminal stenosis of the coronaries. Autopsy studies revealed plaque rupture up to 8-11% in the coronary arteries of patients who died of noncardiac causes and had no history of ischemic heart disease (13,32,33). While plaque ruptures were found up to 16-31% in patients who died of noncardiac causes, but had relevant cardiovascular risk factors (13,31,34). All of the above thoughts strongly suggest that an acute coronary event results as the combination of various factors. Conjunction of certain atherosclerotic plaque characteristics, flow dynamics deviation, intrinsic fibrinolytic and hemostatic dysfunction, neurohormonal dysregulation and external triggers are essential for the initiation of an acute coronary syndrome (13). Additional serial imaging data might contribute to a better understanding of important morphological plaque changes over time.

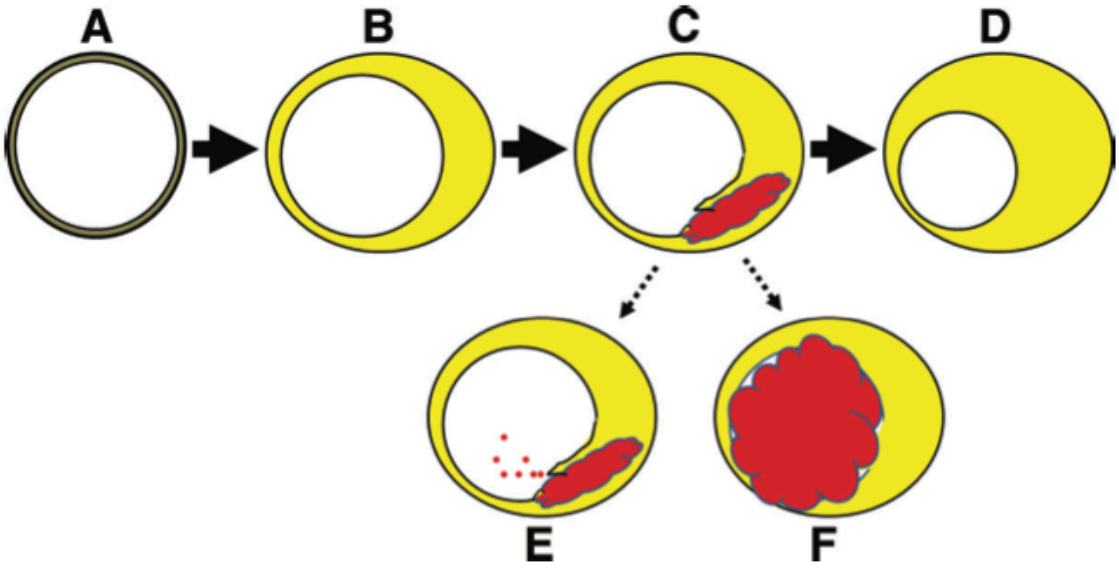

Figure 3 – Evolution of atherosclerotic plaque.

A: normal coronary wall. B: atherosclerotic plaque accumulation with external vascular remodeling and minimal luminal narrowing. C: Plaque rupture with hemorrhage resulting in intramural thrombus. D: Healing of rupture resulting in plaque growth (in the vast majority of the cases). E: Distal embolization of thrombus material (it may cause symptoms or asymptomatic microinfarctions). F: Plaque rupture in coincidence with a thrombosis-conductive state resulting in thrombosis and occlusion of the artery (it may trigger an acute coronary syndrome) (13).

DOI:10.14753/SE.2015.1797

1.2 Imaging of coronary atherosclerotic plaque with CT

Owing to simultaneous data acquisition in numerous parallel slices with sub-second gantry rotation time and data reconstruction with ECG-correlated partial algorithms, coronary computed tomography angiography (CTA) allows for detailed visualization of the moving heart and coronary arteries (35). Thus, it has emerged in the past decade as a powerful tool to detect coronary artery stenosis with excellent sensitivity and good specificity when compared to invasive angiography (17,36,37). Moreover coronary CTA does not only provide data about the luminal narrowing of the coronary artery tree, but also allows the vessel wall to be imaged with high spatial resolution, accordingly permits the characterization of coronary atherosclerotic plaques (38). Current clinical practice of coronary CTA differentiates simply calcified, non-calcified and partially calcified (mixed) atherosclerotic lesions. Although coronary CTA has been shown to be highly accurate in detection of calcified plaque, various studies have demonstrated limitations in visualization of non-calcified plaque (39,40). Yet, growing body of evidence suggests that based on the different computed tomography (CT) attenuation of coronary plaque components, non-calcified plaques can be further distinguished to fibrotic and lipid-rich lesions (17,41). Still, owing to a substantial overlap of the CT numbers of the various plaque types, a reliable differentiation of plaques is not possible with sufficient accuracy (42). Recently, several small studies suggested that a certain morphological pattern on CT, a hyperdense ring-like structure surrounding a hypodense center, described as “napkin-ring” sign (NRS), is associated with advanced coronary plaque as defined by the Amerocan Heart Association (AHA) classification (43-45). Previous studies have shown that the napkin-ring sign in coronary CTA offers a high specificity and positive predictive value to detect lipid-rich plaques, yet the sensitivity of this sign to detect advanced plaque is rather low (43,46,47). This can be related to the various histological characteristics of advanced coronary atherosclerotic lesions resulting in nondescript delineation of the NRS in coronary CT angiography.

Limited detection and characterization of non-calcified coronary atherosclerotic plaques can be further linked to the difficulty to establish outer and inner plaque boundary due to the limited contrast resolution of the CT images, which may have been influenced by

quantum noise (38). Further problem related to image noise is the hampered applicability of automated tools for quantitative coronary CTA assessments, which software packages are available from all CT vendors and several software companies. Automated algorithms have been shown to provide stenosis degree and plaque volume measurements at least as good as manual measurements when compared to gold standard invasive techniques as IVUS (42,48) and they may even reduce inter-/intra-reader variability for the non-calcified plaque quantification, especially for less experienced observers (49). However they are rarely used in clinical practice, as a large portion of automatically fitted boundaries must be manually corrected, which is time consuming and makes reading complicated (42).

Currently, most CT imaging studies have been reconstructed by using the filtered backprojection reconstruction (FBPR) technique. An adaptive statistical iterative reconstruction (ASIR) algorithm was developed to help reduce the quantum noise associated with standard convolution reconstruction algorithms (50,51). Most recently, an algorithm called model-based iterative reconstruction (MBIR) was introduced representing a latest advancement in the field of reconstruction techniques (52). ASIR is a hybrid method, which updates iterative reconstruction technique on FBPR, and MBIR is a raw data based 3-dimensional image reconstruction method, which increases point spread function and thus image resolution. In general, iterative reconstruction techniques have been found to yield lower noise than the FBPR technique (53). Thus, iterative reconstruction techniques may improve the visualization of coronary artery atherosclerotic plaques and have a significant benefit above standard image reconstruction when using automated tools to assess quantitative plaque parameters.

1.3 Imaging of coronary atherosclerotic plaque with MRI

The experience with magnetic resonance imaging (MRI) characterization of carotid artery plaque is now extensive (54). Owing to its excellent soft tissue contrast, MRI is able to differentiate atherosclerotic plaque components, thus detect carotid lipid content, hemorrhage, neovascularization and fibrous cap thickness (55-59). Recently, ultra-short echo time (UTE) MRI has been used to detect and quantify plaque calcification in

carotids (60,61). MRI characterization of coronary plaque, however, is in its nascency. Unlike MRI of the carotids, MRI of the coronary wall currently lacks the spatial resolution needed for the detailed characterization of plaque morphology. High-field MRI systems have been introduced to overcome these difficulties and potentiate high-resolution imaging in human use, however only limited number (approx. 40) of these devices are available worldwide, mostly used for research purposes (62). The challenges with high-field MRI imaging of cardiac structures are magnetic inhomogeneity and specific absorption rate constraints with commercial available high-field at 7T (62). MRI systems are not regularly equipped with required body radiofrequency (RF) transmit coils or surface RF receive coils (62). However, several groups have shown the feasibility of human cardiac imaging with 7T-units, moreover successful imaging of the coronary arteries *in vivo* (62-67). Although these achievements are promising for further clinical use of coronary MRI in the future, the ability of high-resolution MRI to accurately characterize human coronary atherosclerotic plaque remains poorly defined. Only one study to date has examined the correlation between human coronary artery plaque by MRI and histology (68) and this study was hindered by the absence of a sequence to specifically detect plaque calcification.

DOI:10.14753/SE.2015.1797

2 Objectives

2.1 Histopathological correlates of the napkin-ring sign in CT

Our purpose was to identify histological characteristics of advanced coronary atherosclerotic plaques that promote or interfere with the delineation of the napkin-ring sign in coronary CT angiography.

2.2 Plaque visualization with advanced image reconstruction

We aimed to compare the qualitative and quantitative image quality (IQ) parameters of coronary CTA images regarding atherosclerotic plaque visualization in human coronaries with images reconstructed with standard filtered backprojection reconstruction (FBPR), adaptive statistical iterative reconstruction (ASIR) and model-based iterative reconstruction (MBIR) techniques.

2.3 Effect of image reconstruction on automated plaque assessment

We aimed to determine the effect of iterative reconstruction algorithms in comparison to FBPR regarding the need for manual corrections of the automatically fitted vessel-wall boundaries. A reduction of the number of necessary boundary corrections would translate directly into an improved feasibility and potentially into a wider clinical applicability of automated tools for plaque assessment in coronary CTA.

2.4 Characterization of coronary atherosclerotic plaque with MRI

We sought to use high-resolution MRI with T1, T2, and UTE sequences to visualize human coronary atherosclerotic plaques. Furthermore, we aimed to characterize coronary plaques to distinguish potentially vulnerable lipid-rich plaques from more stable fibrocalcific plaques with a high degree of accuracy. In addition, our goal was to assess the capability of MRI to classify human coronary atherosclerotic lesions with T1, T2, and UTE technique as compared to the histopathological plaque classification.

DOI:10.14753/SE.2015.1797

3 Methods

An *ex vivo* experimental setup has been established for the imaging of human coronary atherosclerotic plaques (69). Multimodal imaging techniques (CT and MRI) were used to assess atherosclerotic plaque parameters and compared to co-registered histological data. All procedures were performed in accordance with the local and federal regulations and the Declaration of Helsinki. Approval of the local Ethics Committee was obtained.

3.1 Ex vivo hearts

The human donor hearts were retrieved through the International Institute for the Advancement of Medicine (IIAM). IIAM is a non-profit oriented organization, which facilitates the recovery and placement of donated non-transplantable human organs and tissues with researchers. The donor hearts went through transplantation evaluation, however, the organs deemed unusable or unable to be transplanted mainly due to significant coronary artery disease (CAD).

The donor inclusion criteria according to our protocol were male gender, age between 40 and 70 years, and proven CAD. To minimize the prevalence of coronary segments with chronic total occlusion and severe calcification, donors with long standing diabetes mellitus and/or chronic renal failure were excluded from the study. The maximum warm ischemia time was 6 hours and the maximum cold ischemia time was 15 hours. The fresh donor hearts were transported to our institution in histidine tryptophan-ketoglutarate or University of Wisconsin solution and packed in wet ice. Seven isolated donor hearts (mean age: 53 years, range: 42 – 61 years) were acquired and investigated. The cause of death was stroke in six cases and in one case the cause of death was non-natural (suicide). CAD was proven in all donor hearts either with catheter coronary angiography or based on the donor's medical history.

3.2 Specimen preparation

As a first step, the ascending aorta was removed in order to provide access to the coronary artery ostia. The right and the left coronary arteries were selectively cannulated with plastic luers. The luers were secured in the coronary arteries by ligating the ostial parts from the outer surface of the coronary. After implanting the luers in the coronary arteries, a balloon was placed in the left ventricle and inflated with saline to regain the physiological shape of the ventricle. The following steps were performed on the heart submerged in saline bath. The coronaries were flushed with saline to remove superficial thrombus and air bubbles. As the next step plastic tubes filled with methylcellulose based iodinated contrast agent were attached under water to the luers. The loose ends of the plastic tubes were sealed with a T-port valve. The heart was positioned in the center of a Styrofoam box filled with canola oil to simulate the epicardial adipose tissue compartment. For the MRI analysis formalin pre-fixation was implemented on the specimens. The ostium of the left anterior descending coronary artery (LAD) was selectively cannulated with a catheter with a plastic luer connector, which was connected to a pressure-perfusion system. Buffered neutral formalin solution (10%) was infused at 130 mmHg for 30 min for tissue fixation. A block of myocardium – including the LAD and its proximal side branches – was then excised from the heart for MRI.

3.3 CT Protocol

Methylcellulose based contrast agent (approximately 5-10 ml) was injected in the coronary arteries. To achieve an intra-luminal contrast enhancement similar to *in vivo* CT angiography of the coronary arteries methylcellulose (Methocel, DOW Chemical Company, Midland, MI, USA) with 3% iopamidol contrast agent (Isovue 370, Bracco Diagnostics, Milan, Italy) was used. Typically, with this procedure attenuation within the vessel lumen was achieved similar to *in vivo* studies. CT data acquisitions were performed with a 64-detector row CT scanner (High-Definition, GE Discovery, CT

750HD, Milwaukee, WI, USA) using the following parameters: 64 mm×0.625 mm collimation; 0.35 s rotation time; tube voltage of 120 kV; tube current of 500 mAs.

3.4 CT image reconstruction

The raw data were reconstructed by FBPR, an adaptive statistical iterative reconstruction (ASIR), and a model-based iterative reconstruction (MBIR) algorithm.

FBPR represents the image reconstruction algorithm, which has been used widely during the last years. This method is a discrete implementation of inverse solution of continuous Radon problem so that it can use pre-calculated mathematical solution for an implementation with multiple steps of discretization and approximation (70). As a result, FBPR is easy to implement and fast. However it is still an approximated solution.

In contrast, iterative reconstruction techniques represent an approach where based on true system model (optics or/and geometry) the error between measurements and reconstructed image is minimized (71). In comparison to FBPR, iterative reconstruction algorithms are able to simulate the true X-ray path, in which X-ray photons originate from their location at a focal spot to the detector through the scanned object. The residual error between this forward projection and the scanner-acquired raw projection data is backprojected to update the image, which renders the reconstructed image as the optimum image for the given raw data and system model. Furthermore, iterative reconstruction techniques are able to incorporate noise statistical information of raw projection data and measured electric noise to achieve de-noised images in the final solution with regularization term (71).

Overall, iterative reconstruction algorithms can be classified regarding their extent of implementing information from FBPR. While there are several hybrid iterative algorithms, which include some extent data from FBPR such as ASIR, full iterative reconstruction algorithms, such as MBIR are not yet available in daily clinical practice. Specifically, ASIR predominantly focuses on the modeling of the statistical behavior of incident photons and electric noise (so called statistical modeling) and is limited to a number of iterations. It compares image data to a noise model to improve image quality

(72). A blending factor of 40% was chosen for ASIR based on the recommendation from the vendor. Image reconstruction was performed at the workstations of our department's console.

MBIR is a full model-based iterative reconstruction algorithm that implements data from modeling the actual detector response function, the focal spot size, and the system geometry (so called system optics modeling) along with statistical behavior of incident photons and electric noise (so called statistical modeling) (52,72,73). This algorithm is more computer-intensive due to multiple iterations from raw data based image reconstruction and so far not available for coronary CTA. Therefore, an *ex vivo* setting was chosen and a prototype version of this algorithm was applied at the research department of the vendor (GE Healthcare, Milwaukee, WI, USA).

All images were reconstructed at 0.625 mm slice thickness, 0.4 mm slice increment, and full field of view with FBPR, ASIR, and MBIR techniques by using soft-tissue kernel. All reconstructed CT images were sent to an offline workstation for further analysis.

3.5 MRI Protocol

Magnetic resonance images were acquired on a 9.4T horizontal bore magnetic resonance scanner (Biospec, Bruker, Billerica, MA, USA) using transmit-receive birdcage coil. The specimens were immersed in a fluorocarbon-matching medium with the same magnetic susceptibility as tissue but no proton MRI signal, thus providing a signal and artifact free background (Fomblin, Ausimont, NJ, USA). Specimens were imaged with T1, T2 and UTE sequences. T1-weighted imaging was achieved with a 3 dimensional (3D) gradient echo sequence using the following parameters: field of view (FOV) 48x36x64mm^3, image matrix 192x144x256 (0.250mm isotropic resolution), TR = 30ms, TE = 2.5ms, flip angle 45 degrees, fat suppression, 1 average. T2-weighted imaging was performed using a 2 dimensional (2D) fast spin echo sequence with the following parameters: FOV 40x30mm^2, image matrix 256x192 (in plane resolution 0.156 mm), slice thickness 0.4 mm, TR = 3000 ms, TE = 40 ms, echo train 16, 16 averages. UTE imaging was performed using a 3D radial sequence with the following parameters: FOV 51x26x60 mm^3, image matrix 192x192x192

DOI:10.14753/SE.2015.1797

(resolution 0.267x0.133x0.312 mm^3) projections 75546, TR = 8 ms, TE = 20 μs, fat suppression, 1 average.

3.6 Histopathology

The histological processing and analysis was performed at a pathology institute specialized in cardiovascular histopathology (CV Path Laboratory, Maryland, MD, USA). The coronary specimens were embedded en bloc in paraffin. Cross-sections were acquired in 1-mm increments (6μm slice thickness) and Movat's pentachrome staining was used according to the standard techniques (74). Images were digitalized using a high-resolution camera attached to a microscope connected to a PC workstation and converted into high-resolution TIFF images. An experienced pathologist blinded to the CT and MRI data analyzed the histological sections. Main plaque components such as lipid-rich necrotic core and calcification were reported. Further classification of the coronary plaques was performed according to the histological criteria established by the AHA (4). Each cross-section was classified according to the AHA classification and early and advanced lesions were distinguished.

For the assessment of the napkin-ring sign, all plaques that were previously classified as advanced were further analyzed regarding the presence or absence of a lipid-rich necrotic core (LRNC), intraplaque hemorrhage, intraplaque microvessels, macrophage infiltration and calcifications. The latter characteristics were stratified as being related or unrelated to the lipid/necrotic core. Calcifications were subdivided into micro-calcifications (punctate calcification of smooth muscle cells, macrophages, or extracellular matrix, maximum diameter <50 μm), spotty (coalescent calcification, maximum diameter 50-1000 μm) and sheet calcifications (plate calcification, maximum diameter >1000 μm) (75). All cuts that were subsequently digitalized were further analyzed using dedicated software and manual contouring (ImageJ 1.44o, National Institutes of Health, Bethesda, MD, USA).

Vessel area (VA) was defined as the area inside the external elastic lamina. Furthermore, the lumen area (LA) and the area of the lipid/necrotic core (CA) were measured. From this data, the total plaque area (TPA) was calculated as TPA = VA – LA. The area of non-core plaque was calculated as NcA = TPA – CA. The plaque burden (PB) was calculated using the following formula: PB = (TPA / VA) * 100. We also assessed the thickness of the fibrous cap, which was measured at its thinnest part.

Histologic features representing the atherosclerotic plaque such as size and area of the necrotic core and area of non-core plaque as well as the presence of calcification, hemorrhage and macrophages are further referred to as histologic plaque features.

Variables associated with the plaque such as the vessel area, the lumen area, plaque burden and distance of the plaque from the ostium are further referred to as associated plaque features.

3.7 Co-registration of the images (CT, MRI, histology)

All images were co-registered using a freeware Dicom reader (OsiriX, version 3.6.1, Geneva, Switzerland) by an experienced investigator, who was not participating in further image analysis.

A multiplanar reconstruction technique was used to generate CT images perpendicular to the vessel centerline to match the position of the histological cuts prepared in 1-mm increments. The cross-sectional and rotational position of the slices were identified by distance measurements from the distal end of the plastic cannulas and verified by using fiducial markers such as side branches, bifurcations and features of vessel wall morphology (e.g.: plaque shape, calcification pattern, orientations of the myocardium and the pericardial adipose tissue layer).

The cross-sectional images were co-registered between FBPR, ASIR, and MBIR similarly by using the distance from the plastic luer as a fixed starting point. Furthermore, plaque burden profiles were generated for each vessel and compared between the different reconstruction algorithms to guarantee perfect alignment of each coronary cross-section in the co-registered dataset.

Manual co-registration of the T1, T2, and UTE MRI data with the CT images and histological slides was performed by using multi-planar reformats of the MRI images perpendicular to the vessel centerline prepared in 1-mm increments to match to the histological slides. Anatomical features such as distance from the coronary ostia, presence of side-branches or vessel bifurcation, vessel size and shape, and plaque morphology were used to warrant the rigid co-registration.

DOI:10.14753/SE.2015.1797

3.8 CT analysis

3.8.1 Features associated with the napkin-ring sign

As the most advanced, model-based image reconstruction technique is available mostly in the research phase, the dataset used for plaque feature assessment was reconstructed using ASIR technique. The purpose of this sub-study was to define features of advanced atherosclerotic plaques that promote or interfere with the delineation of the NRS in coronary CT angiography, thus, only cross-sections containing advanced plaques as classified by histology were used. The corresponding CT images were reviewed in consensus by two radiologists with 6 and 10 years of experience in coronary CT angiography. All reading was performed using a fixed window setting [700 Hounsfield Units (HU) width, 200 HU level]. Based on the CT appearance, it was specified whether a napkin-ring sign could be identified within the plaque. The NRS was defined by a low-attenuation plaque core surrounded by a circumferential area of higher attenuation (45). Additionally, we measured the attenuation of the non-calcified plaque portion of all plaques using an in-house program developed in Matlab. For this purpose, the outer circumference of the vessel and the lumen were manually traced and the median density of the pixels within the plaque was calculated. In plaques with a positive NRS, we also measured the median density of the central hypodense area and the peripheral hyperdense ring.

3.8.2 Image quality of different reconstruction techniques

Image analysis was performed at a commercially available workstation (Advantage Windows 4.2; GE Healthcare, Milwaukee, WI, USA) by two experienced observer blinded to the image review results. The three image sets, obtained with reconstruction techniques FBPR, ASIR, and MBIR in each patient, were displayed side by side with a preset soft tissue window (window width, 200 HU; window level, 700 HU).

3.8.2.1 Qualitative image analysis

The two reviewers were asked to grade the overall image quality on a four-point scale: 1 = excellent; 2 = good (minor artifacts); 3 = moderate (considerable artifacts but diagnostic quality); 4 = poor, non-diagnostic. Regarding calcification and blooming artifacts, both readers were asked to rate if there is calcification or not. If present, a three-point scale was used to qualify blooming artifacts: 0 = no blooming; 1 = blooming but lumen clearly visualized; 2 = blooming, no lumen visible. Image noise was defined as overall graininess or mottle in the coronary artery. It was graded on a four-point scale: 1 = no image noise; 2 = average noise; 3 = above average noise; 4 = severe noise. Image sharpness was evaluated on a five-point scale: 0 = extremely poor, no definable lumen; 1 = poor, severe streaking comprising more than 50% of the vessel lumen; 2 = fair, vessel walls may show mild streaking or blurring, but a defined lumen is identifiable; 3 = good, coronary walls may be blurred but lumen is clearly discernible and separate from the surrounding fat; 4 = excellent, coronary walls are sharp and well-defined with no blurring. Such an assessment scheme was used in a previous study of coronary lumen analysis at CT (76,77).

3.8.2.2 Quantitative image analysis

We obtained mean CT attenuation values (in Hounsfield units) for the peri-coronary fat and coronary artery by manually placing circular regions of interest (ROIs) at the same image level. The attenuation of the coronary artery was recorded from a single drawn ROI that was as large as the vessel lumen. For each protocol, image noise was measured as the standard deviation of the pixel values from a circular or ovoid ROI drawn in a homogeneous region of the peri-coronary fat. For all measurements, the size, shape, and position of the ROIs were kept constant among the three protocols by applying a copy and paste function at the workstation. The attenuation of the peri-coronary fat was recorded as the measurement of one ROI placed in the peri-coronary area to the coronary lumen. Areas of focal changes in parenchymal attenuation and prominent artifacts, if any, were carefully avoided. For each of the three reconstructions, the

contrast-to-noise ratio (CNR) relative to peri-coronary fat for the coronary artery was calculated by using the following equation: $CNR = (HU_{lumen} - HU_{fat}) / SD_{lumen}$, where HU_{lumen} and HU_{fat} are the mean CT numbers of the coronary artery lumen and the peri-coronary adipose tissue, respectively. SD_{lumen} represents the standard deviation of luminal CT number.

3.8.3 Automated plaque assessment

For each vessel reconstructed by three different algorithms (FBPR, ASIR, MBIR), a separated 3D dataset was generated. All images were anonymized regarding the applied reconstruction algorithm and vessel origin. All 3D datasets were transferred to a dedicated offline workstation (Vitrea Advanced Cardiac Solutions, Vital Images, Minnetonka, MN, USA), which allowed automated vessel segmentation and quantification of coronary artery components (49,78).

The starting point for the luminal centerline was manually set at the proximal ending of the vessel by a coronary CTA reader in the 3D dataset and visually verified. Afterwards, the software performed the automatic vessel segmentation and fitted the inner and outer vessel-wall boundaries. The automatically fitted boundaries were reviewed by an experienced coronary CTA reader on cross-sectional images with 0.5 mm increments. If the boundaries did not follow the anatomical structures, the inner and/or outer vessel-wall boundary was manually corrected. The proximal 40 mm of each vessel (left anterior descending [LAD], left circumflex [LCX], right coronary [RCA] artery) starting from the plastic luer was included in the assessment, plus the left main (LM) which was counted as part of the LAD. All measurements were exported for further processing.

The primary endpoint was the percentage of cross-sections where a manual correction of the automatically fitted vessel-wall boundaries (inner or outer) was necessary to perform. Secondary endpoints were the following: 1.) Percentage of cross-sections that required corrections of only the inner vessel-wall boundary; 2.) Percentage of cross-sections that required corrections of only the outer vessel-wall boundary; 3.) Benefit of MBIR over FBPR (or over ASIR), which was defined as cross-sections that needed any

corrections on FBPR (or ASIR) but not in MBIR, as compared to cross-sections, which showed no difference between MBIR and FBPR (or ASIR). The latter group contained cross-sections which have been or which have not been corrected in both image reconstruction algorithms (MBIR and FBPR; MBIR and ASIR).

The reproducibility of the primary endpoint was confirmed in a random subset (33% of the entire cohort). The vessel assessment including the boundary delineation was performed twice with a time gap of two weeks. A high correlation was observed with respect to the percentage of corrected cross-sections per vessel between the two assessments (intraclass correlation coefficient: 0.99). Also, an excellent regional agreement was achieved comparing which individual cross-sections were corrected the first and second time (kappa: 0.86).

3.9 MRI image analysis

Prior to data analysis a 5-point image quality Likert-type scale was used to assess the quality of the UTE images (57). UTE images with a clearly definable lumen, coronary wall and adventitial boundary, and with no artifacts were graded as 5; those with minor artifacts were rated as 4; grade 3 was assigned to images where the wall structures were easily identifiable, but the lumen and outer boundaries were partially obscured. Non-diagnostic images were assigned a grade 2 if only the arterial wall was distinct, and grade 1 if no structures were visible. Two independent, experienced cardiac imaging specialists rated the IQ.

Three independent observers blinded to the histological plaque classification performed plaque classification. In cases of disagreement a consensus was reached in a subsequent reading. The MRI signal and contrast characteristics used to identify the relevant plaque components are shown in **Table 1**. Areas of plaque showing signal hypointensity on the T1 but not on the UTE images were classified as calcified. Areas showing signal hypointensity on the T2 images were classified as lipid-rich necrotic core. Hemorrhage was identified by hyperintensity on the T1 and UTE images and regions that were isointense on all sequences were classified as fibrotic, **Table 1**. Signal intensities were interpreted with the adjacent myocardium as a reference.

Table 1 – Predicted signal intensities of plaque components by MRI.

	Ca	LRNC	Fibrotic	Hemorrhage	Tissue Tear/ Disruption*
T1	Hypo	Iso	Iso	Hyper	Hypo
T2	Hypo	Hypo	Iso	Hyper/Hypo	Hypo
UTE	Iso	Iso	Iso	Hyper	Hypo

Ca = calcification, Hypo = hypointense, Iso = isointense, Hyper = hyperintense

* Results in the local accumulation of the fluorocarbon matching medium

The used MRI classification system (**Table 2**) was based on the one that has been proposed by Cai et al. for carotids (79), but was adopted to include the assessment of plaque calcification using the UTE technique (60,61). Type I and II lesions were grouped together (I-II lesions) and defined by slight thickening of the arterial wall with near normal wall thickness. Type III plaque was defined by eccentric wall thickening. Type IV and V lesions were grouped together, as per the Cai classification, but were further subclassified by UTE MRI as being either non-calcified IV-VA or calcified IV-VB. The presence of a surface defect and/or luminal thrombus (type VI plaque) is challenging to detect accurately *ex vivo*. Thus, we did not include a separate category for these plaques in our classification scheme. Type VII lesions (completely calcified plaque) were included in the analysis but where not encountered. Type VIII lesions were defined as per Cai et al as highly fibrotic, but could be further subclassified by UTE MRI as being either non-calcified VIIIA or calcified VIIIB.

Table 2 – Scheme for classification of atherosclerotic plaques with MRI (4,59).

Conventional AHA classification [4]	**Modified AHA classification for MRI** [59]	**Modified AHA classification for MRI adopted for UTE imaging**
Type I: initial lesion with foam cells	**Type I-II:** near normal wall thickness, no calcification	**Type I-II:** near normal wall thickness, no calcification
Type II: fatty streak with multiple foam cell layers		
Type III: preatheroma with extracellular lipid pools	**Type III***:* diffuse intimal thickening or small eccentric plaque with no calcification	**Type III:** diffuse intimal thickening or small eccentric plaque without calcification
Type IV: atheroma with a confluent extracellular lipid core	**Type IV-V***:* plaque with a lipid or necrotic core surrounded by fibrous tissue with possible calcification	**Type IV-VA:** plaque with lipid or necrotic core surrounded by fibrous tissue without calcium
Type V: fibroatheroma		**Type IV-VB:** plaque with lipid or necrotic core surrounded by fibrous tissue with calcium
Type VI: complex plaque with possible surface defect, hemorrhage or thrombus	**Type VI:** complex plaque with possible surface defect, hemorrhage or thrombus	**Type VI:** complex plaque with possible surface defect, hemorrhage or thrombus
Type VII: calcified plaque	**Type VII:** calcified plaque	**Type VII:** calcified plaque
Type VIII: fibrotic plaque without lipid core	**Type VIII:** fibrotic plaque without lipid core and with possible small calcifications	**Type VIIIA:** fibrotic plaque without lipid core and without calcification
		Type VIIIB: fibrotic plaque without lipid core and with calcification

AHA: American Heart Association

3.10 Statistical analysis

Continuous variables are reported as mean (standard deviation) or median [interquartile range] and categorical by percentage (counts). Statistical analysis was performed using commercially available software (SAS, version 9.2 SAS Institute Inc., Cary, NC, USA). A p-value of <0.05 was considered significant.

3.10.1 Napkin-ring sign

In univariate analysis, we tested which parameters derived from histology were significantly different between sections with and without NRS in CT. Wilcoxon signed-rank test and Fishers exact test were used to assess differences within continuous and categorical variables. All variables which showed a difference at a significance level of $p<0.01$ were included in multivariate analysis. We fitted two different logistic regression models, one for associated variables and one for histologic variables. Non-significant variables were removed stepwise from the initial models. The remaining significant variables from both models (associated and histologic) were combined in a final multivariate logistic regression model. We derived from these models the c-statistic, which is equal to the area under the curve. To estimate the probability of NRS appearance in dependency of the necrotic core size, we fitted a univariate logistic regression model where the necrotic size served as the predictor.

To assess the inter-observer variability of the measurements in the histology sections, the measurements were repeated by a second reader in a subset of 30 randomly chosen histology slices. The agreement between the two readers was evaluated using Pearson correlation coefficients and calculation of relative differences. A paired t-test was performed to assess whether the difference varied significantly from zero.

To determine inter-observer variability for the detection of the napkin-ring sign, an independent reader assessed a random subset of 100 co-registered coronary CTA images for the presence of the napkin-ring sign. The inter-observer agreement was evaluated using Cohen's kappa statistics that was interpreted as follows: A κ value

greater than 0.80 corresponded to an excellent agreement, a κ value of 0.61-0.80 good inter-observer agreement, and a κ value of 0.41-0.60 moderate agreement (80).

3.10.2 Image quality

The observer-agreements regarding qualitative parameters (i.e. presence of calcifications, image quality, image noise score, sharpness) between readers and readouts were analyzed by using weighted kappa. The Mantel-Haenszel Chi^2-test was used to compare categorical parameters between the reconstruction techniques and between images with and without calcifications.

The inter- and intra-reader agreement between quantitative parameters (i.e. luminal CT number, image noise, CNR) was assessed using Pearson's correlation coefficient. Comparisons of quantitative parameters between reconstruction techniques was carried out using ANalysis Of VAriances, t-test for related samples was used for pairwise comparisons. Spearman's correlation analysis was used to correlate image noise as assessed quantitatively with the qualitative image noise score.

3.10.3 Automated plaque assessment

Chi-square test was used for categorical and t-test for continuous variables compared between cross-sections with versus those without any boundary corrections.

The percentage of cross-sections with boundary corrections per vessel was compared between FBPR, ASIR and MBIR using a paired Wilcoxon Rank-sum test. To assess the regional agreement of performing boundary corrections, Cohen's kappa statistics was calculated between FBPR, ASIR, and MBIR.

To assess the association of co-variates to the benefit of MBIR over FBPR (or ASIR) multivariate logistic regression analysis was applied. As co-variates, minimal luminal diameter, plaque area and burden as well as the extent of calcification were included in the model, as derived from MBIR datasets. The extent of calcification was defined based on relative plaque volumes: no calcification equaled to 0% of plaque volume

≥180 HU, moderate calcification to 1-24% of plaque volume ≥180 HU, severe calcification to ≥25% of plaque volume ≥180 HU (81).

The intra-reader reproducibility was determined for the primary endpoint; the assessment was repeated with a time gap of two weeks in a random sub-set (n=9 vessels) of vessels reconstructed with FBPR, ASIR, or MBIR. The reproducibility was assessed using intraclass correlation coefficient (ICC) and Cohen's kappa statistics.

3.10.4 MRI

Continuous variables with normal distributions are expressed as mean ± standard deviation, while categorical variables are given as counts and percentages.

Inter-observer agreement for image quality rating was assessed using Spearman's rank correlation. Inter-observer agreement for plaque classification was determined by using kappa statistic as reported previously (82). Using histology as the gold standard, the sensitivity, specificity, positive, and negative predictive values (plus binominal 95% confidence intervals) of MRI for the detection of calcium and lipid-rich necrotic core were calculated. The agreement between MRI classification and the gold standard histology was calculated using weighted kappa.

DOI:10.14753/SE.2015.1797

4 Results

4.1 Histopathological correlates of the napkin-ring sign plaque in CT

4.1.1 Histological characteristics of the napkin-ring sign

Based on the histopathological evaluation, advanced plaques (types IV-VI) were present in 139 (22.7%) of 611 cross-sections, while early lesions were found in 472 slices (77.3%). Among the advanced lesions 33 (23.7%) demonstrated an NRS in coronary CTA, whereas no NRS was found in 106 slices (76.3%), see **Table 3** and **Figures 4** and **5**. However, NRS was also found in 5 of the 472 slices (1.1%) classified as early lesions.

Table 3 – Distribution of histologic features in plaques with positive and negative NRS on coronary CT angiography.

	NRS (n=33)	Non-NRS (n=106)	*p*-value
Lipid-rich necrotic core *related* components			
Macrophages	18 (55%)	48 (45%)	0.43
Angiogenesis	16 (48%)	32 (30%)	0.06
Hemorrhage	11 (30%)	25 (24%)	0.27
Micro-calcification	9 (27%)	49 (46%)	0.07
Spotty or sheet calcification	14 (42%)	31 (29%)	0.20
Lipid-rich necrotic core *unrelated* components			
Macrophages	1 (3%)	7 (7%)	0.68
Angiogenesis	4 (12%)	26 (25%)	0.15
Hemorrhage	2 (6%)	7 (7%)	1.00
Micro-calcification	2 (6%)	10 (9%)	0.73
Spotty or sheet calcification	1 (3%)	18 (17%)	0.04
Additional lipid pool	4 (12%)	37 (35%)	0.02

DOI:10.14753/SE.2015.1797

The napkin-ring sign was most commonly observed in the right coronary artery (55%) followed by the left-circumflex artery (30%) and the left anterior descending artery (15%). In contrast, plaques without NRS were evenly spread among the 3 arteries. The median density of the non-calcified plaque portion was 61.8 HU [48.4-70.1 HU] for plaques with an NRS and 65.9 HU [49.3-87.7 HU] for plaques without NRS (p=0.10). In plaques with a positive NRS, the median HU of the central hypodense area was 48.1 HU [33.4-61.6 HU], whereas the rim showed a median density of 68.2 HU [52.3-76.5 HU]. The difference between the density values was significant (p<0.001).

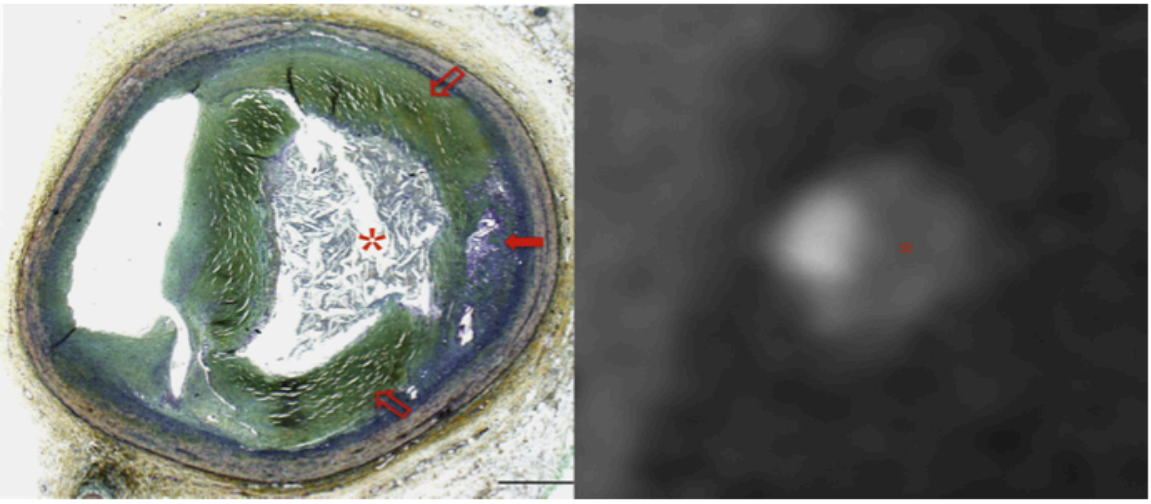

Figure 4 – (Late) fibroatheroma as classified by histology.

Note the large necrotic core (*) in the center of the plaque in the histology image (left image), which correlates with the hypodense center of the plaque (*) in CT (right image). The core is surrounded by prominent fibrotic tissue (open arrows), which appears as a hyperdense ring around the core in CT. Thus the plaque has a ring-like appearance in coronary CTA which was coined as napkin-ring sign. Additionally neovascularization is present within the plaque (closed arrow).

DOI:10.14753/SE.2015.1797

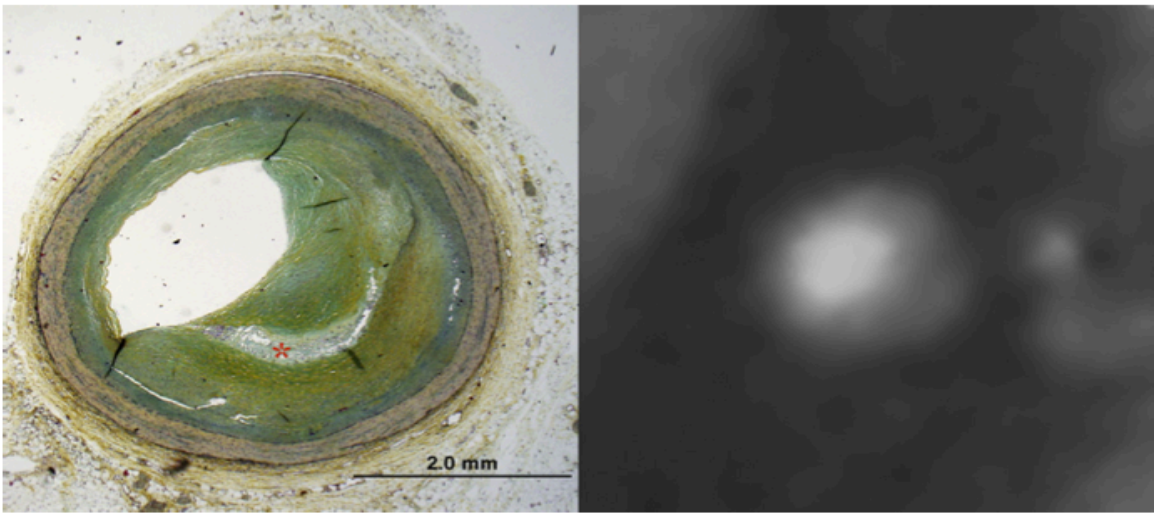

Figure 5 – (Early) fibroatheroma as classified by histology.

Note the small lipid core in the histology image (left image). Due to the small size, the lipid core (*) did not appear as a napkin-ring sign in coronary CTA.

4.1.2 Histologic features corresponding to the napkin-ring sign

The frequency of histologic plaque features and their relation to the presence or absence of NRS on CT is summarized in **Table 3**.

The area of the necrotic core was more than twice as large in plaques with NRS as compared to those without NRS (median 1.1 mm^2 vs. 0.5 mm^2, p=0.05, **Figure 6**). Similarly, the area of non-core plaque was significantly larger in plaques with NRS as compared to those without (median 10.2 mm^2 vs. 6.4 mm^2, p<0.001, **Figure 6**). The thickness of the fibrous cap was not different for plaques with and without NRS (median 0.4 mm vs. 0.3 mm, p=0.15). Microvessels within the plaque, indicative of angiogenesis tended to be more frequent in plaques exhibiting the NRS sign (48% vs. 30%, p=0.06), while microcalcifications tended to be more common in plaques without an NRS (27% vs. 46%, p=0.07). The presence of macrophages, hemorrhage, and calcifications (independent of whether they were spotty or sheet-like) in close proximity to the lipid core was not associated with the NRS. Additional lipid pools, smaller than the main core, were more common in plaques without an NRS (35% vs. 12%, p=0.02) Histologic plaque features distant from the core were generally not associated with the NRS except for core-unrelated spotty and sheet calcifications, which were more commonly detected in the absence of an NRS (3% vs. 17%, p=0.04).

In multivariate adjusted analysis the area of the necrotic core [OR: 1.70 (95% CI: 1.12-2.57 per increase by one mm^2, p=0.01] and the area of the non-core plaque [OR: 1.24 (95% CI: 1.11-1.40) per increase by one mm^2, p<0.01] remained as independent predictors of the NRS. In contrast, the presence of additional smaller lipid pools independently reduced the probability of the appearance of the NRS [OR: 0.22 (95% CI: 0.07-0.75)].

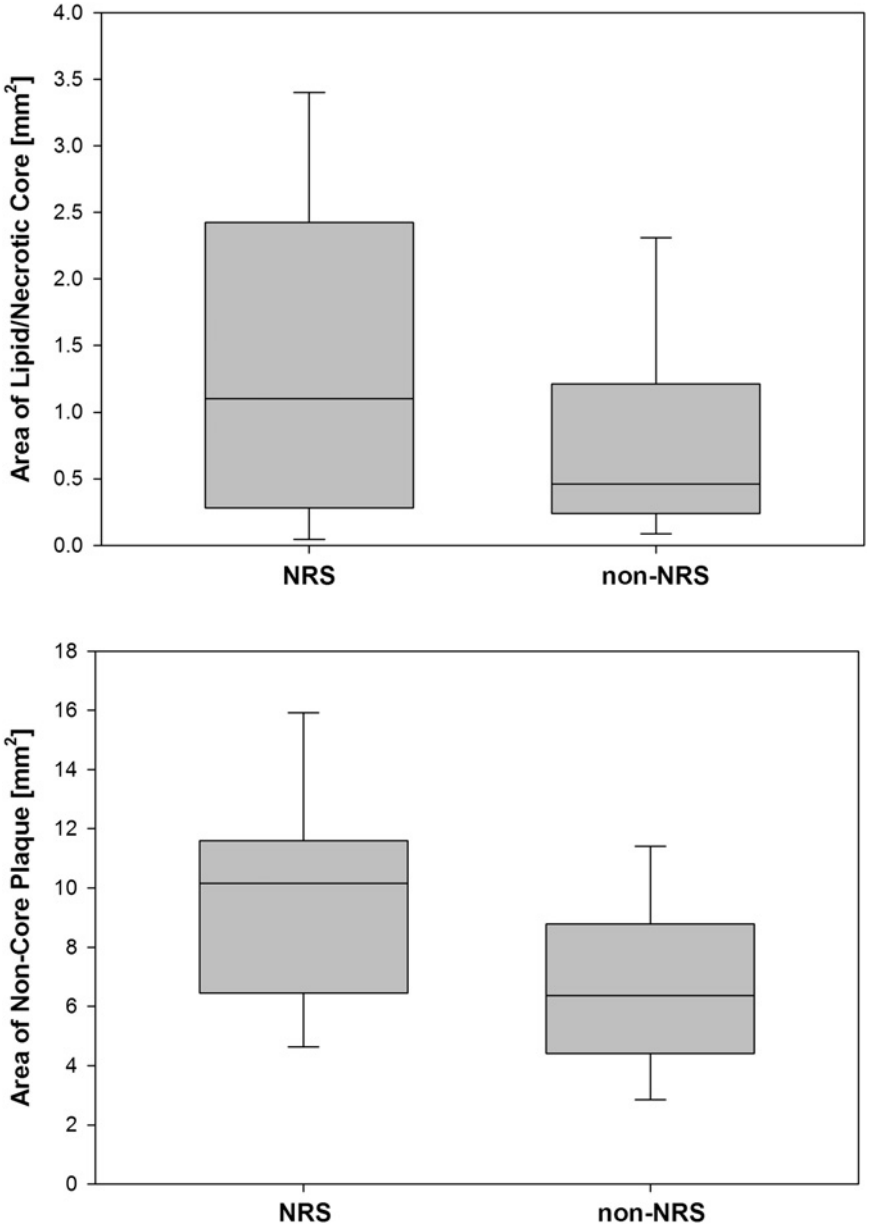

Figure 6 – Areas of the lipid/necrotic core and the non-core plaque as measured in histology in plaques with presence and absence of the napkin-ring sign in coronary CTA.

Although there is a substantial overlap, the mean size of the core was significantly larger in plaques with positive NRS. Note that the vast majority of cores in plaques without the NRS had an area below 1 mm^2, which is deemed a crucial size often found in rupture-prone lesions. Plaques with a positive NRS in coronary CT angiography also had a significantly higher non-core plaque area as compared to plaques without the NRS.

4.1.3 Other features associated with the napkin-ring sign

Plaques exhibiting a NRS on CT were located more proximally as compared to those without NRS (median distance from ostium 19.0 mm vs. 31.0 mm, respectively; p=0.02). Also, the vessel area was larger at the site of the plaque (median 17.1 mm^2 vs. 12.9 mm^2, p=0.02) and plaque area itself was larger (median 11.5 mm^2 vs. 7.5 mm^2, p<0.001) in plaques with NRS than in plaques without NRS. Interestingly, the lumen area was not different between plaques with and without NRS (median 2.6 mm^2 vs. 3.1 mm^2, p=0.58). As a result, plaque burden was significantly larger in plaques with NRS as compared to those without NRS (80% vs. 69%, p<0.001).

In multivariate adjusted analysis both vessel area [OR: 0.84 (95% CI: 0.75-0.94) per 1 mm^2 increase, p<0.01)] and plaque area [OR: 1.74 (95% CI: 1.36-2.21) per 1 mm^2 increase, p<0.0001] remained independent predictors for the delineation of the NRS in CT. Plaque burden was not included in this analysis as it was co-linear and inferior to the combination of vessel and plaque area.

When adjusting for both histologic and associated features the area of the necrotic core area, the area of the non-core plaque, and the vessel area remained independent predictors for the appearance of the NRS with the area of the necrotic core being the strongest predictor (OR 1.91; 95% CI: 1.23-2.98). The combined model reached a c-statistic of 0.816, **Table 4**.

Table 4 – Independent predictors of the napkin-ring sign.

Independent predictors	OR (95%CI)	*p*-value
Vessel area [per mm^2]	0.88 (0.78-0.99)	0.03
Area of non-core plaque [mm^2]	1.60 (1.24-2.05)	0.0002
Area of lipid and/or necrotic core [mm^2]	1.91 (1.23-2.98)	0.004
Presence of additional lipid cores	0.36 (0.10-1.25)	0.11

4.1.4 Interobserver-agreement

We found a very good correlation between the measurements for the vessel area, lumen area and the area of the necrotic core (r=0.998, 0.994, and 0.997 respectively) in histology. Measurements for necrotic core area and vessel area were significantly different between the two readers ($p<0.05$), however, the mean difference between the measurements was 1.9% (0.3±0.5 mm^2) for the vessel area and 2.9% (0.04±0.08 mm^2) for the area of the necrotic core. No difference was found between the two readers for the lumen area (p=0.61).

The interobserver agreement between the two CT readers to detect the napkin ring sign was excellent (Cohen's kappa=0.86; 95% CI: 0.76-0.96).

DOI:10.14753/SE.2015.1797

4.2 Impact of CT image reconstruction on coronary plaque visualization

A total of 1125 images were used for this sub-analysis derived from three datasets reconstructed with FBPR, ASIR, and MBIR yielding 375 triplets of co-registered image sets. All of these were included in image quality analysis.

4.2.1 Qualitative image analysis

Kappa-values indicated good to excellent inter- and intraobserver agreement regarding qualitative parameters except for image sharpness (κ=0.38), **Table 5**. Although both readers had full agreement only in 43% of the cases regarding image sharpness, both were only a single category apart using a 5-point Likert scale in 54% of the cases.

Table 5 – Inter- and intra-observer agreement for qualitative parameters.

	Inter-observer		**Intra-observer**	
	Kappa	Agreement	Kappa	Agreement
Image quality	0.92	>90%	1.00	>90%
Calcification	0.73	85%	0.97	>90%
Blooming	0.47	70%	0.89	>90%
Image noise score	0.62	74%	0.92	>90%
Sharpness	0.38	43%	0.91	>90%

Overall image quality was classified to be good or excellent in 274 (73.1%) and 48 (12.8%) images using FBPR, 318 (84.8%) and 15 (4.0%) images using ASIR, and 248 (66.1%) and 96 (25.6%) using MBIR, **Figure 7**. Image quality was significantly better with MBIR than with ASIR ($p<0.001$) or FBPR ($p<0.001$). ASIR and FBPR reconstruction techniques yielded similar image quality ($p=0.17$).

Calcifications were observed in 369/1125 images (32.8%), no significant differences were discovered among the three reconstruction algorithms (FBPR, 33.9%; ASIR,

32.8%; MBIR, 31.7%; p = 0.53). Independent of the CT image reconstruction technique, image quality was significantly ($p<0.001$) worse if calcification was present. Regarding images with presence of calcifications, 87/369 images (23.6%) were considered to show no blooming, 267/369 images (72.4%) were considered to have blooming artifacts but allowing luminal visualization, and 15/369 images (4.1%) were considered to have blooming artifacts rendering luminal visualization impossible. No differences among FBRR, ASIR, and MBIR were revealed ($p=0.95$), **Figure 8a–c**.

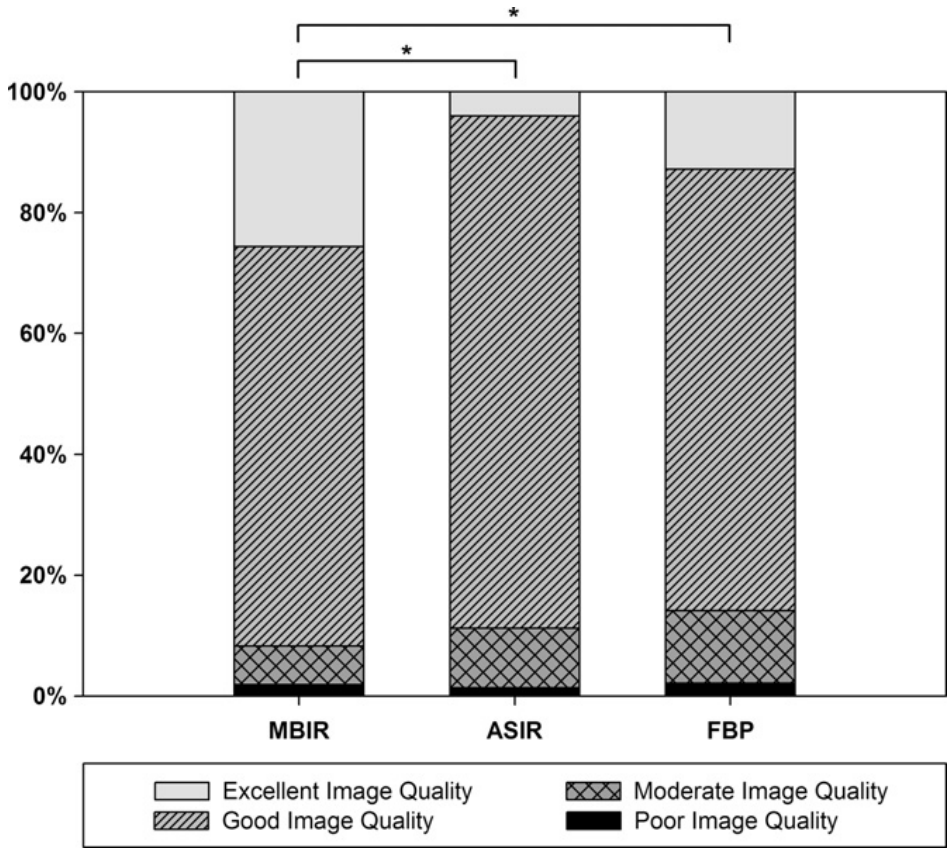

Figure 7 – Overall image quality as assessed by qualitative analysis.

Image quality was significantly better with MBIR than with ASIR (*$p<0.001$) or FBPR (*$p<0.001$). ASIR and FBPR reconstruction techniques yielded similar image quality ($p=0.17$).

DOI:10.14753/SE.2015.1797

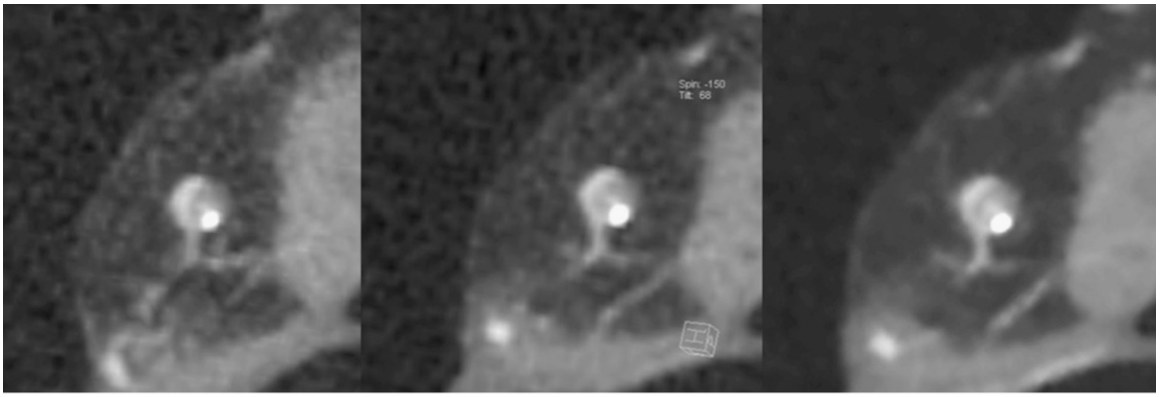

a b c

Figure 8 – Cross-sectional CT images of a partially calcified atherosclerotic plaque.

CT images reconstructed with (a) FBPR, (b) ASIR, and (c) MBIR technique. There is no difference in blooming of calcified component of the coronary artery plaque in the three different reconstruction modes.

Regarding image noise score the majority of images were rated to be of score 3, using in 325 images (86.7%) reconstructed with FBPR, and 296 (78.9%) images reconstructed with ASIR. Regarding the reconstruction technique of MBIR, images were most frequently classified to be of image noise score 2 representing 231 (61.6%) of the cases. Image noise was significantly lower by ASIR as compared to FBPR ($p<0.01$) and was further reduced by MBIR as compared to ASIR ($p<0.001$, **Figure 9**).

DOI:10.14753/SE.2015.1797

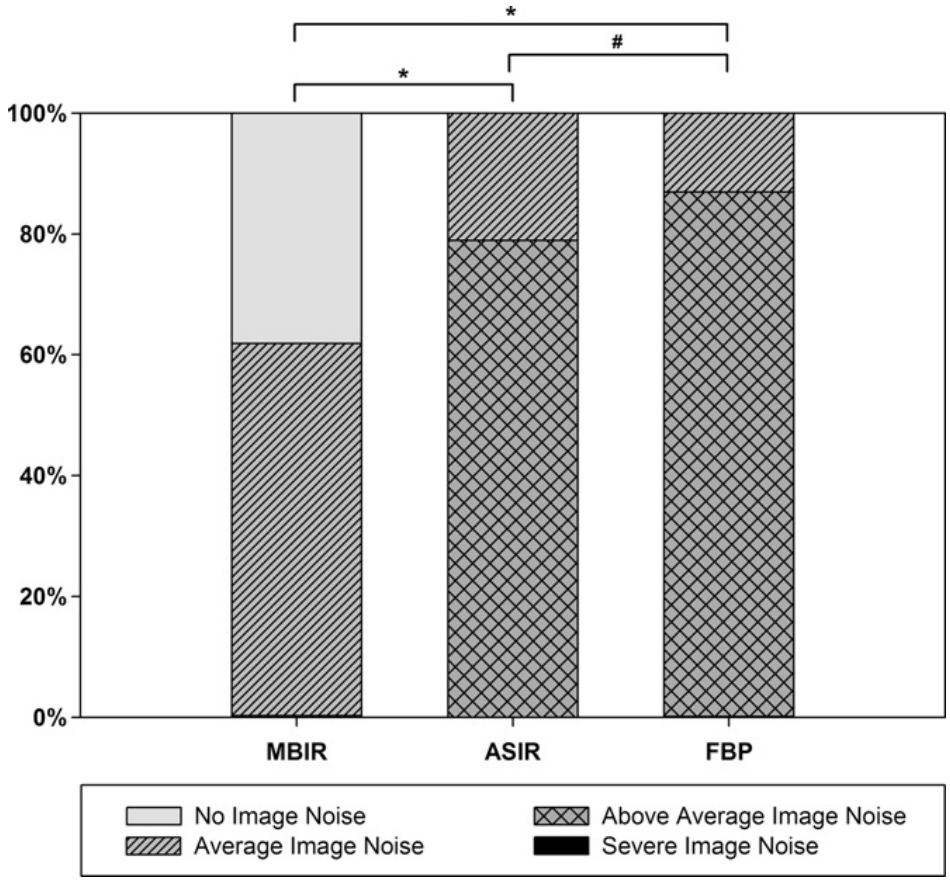

Figure 9 – Image noise as assessed by qualitative analysis.

Image noise score was significantly lower by ASIR as compared to FBPR ($^{\#}p<0.01$) and was further reduced by MBIR as compared ASIR (*$p<0.001$).

Image sharpness with MBIR was significantly improved as compared to ASIR ($p<0.001$) and FBPR ($p<0.001$); however, ASIR and FBP were comparable ($p=0.61$). Percentages representing the different image sharpness categories are demonstrated in **Figure 10.** Examples for the differences in image sharpness and image noise between the three reconstruction algorithms are shown in **Figure 11a–c**.

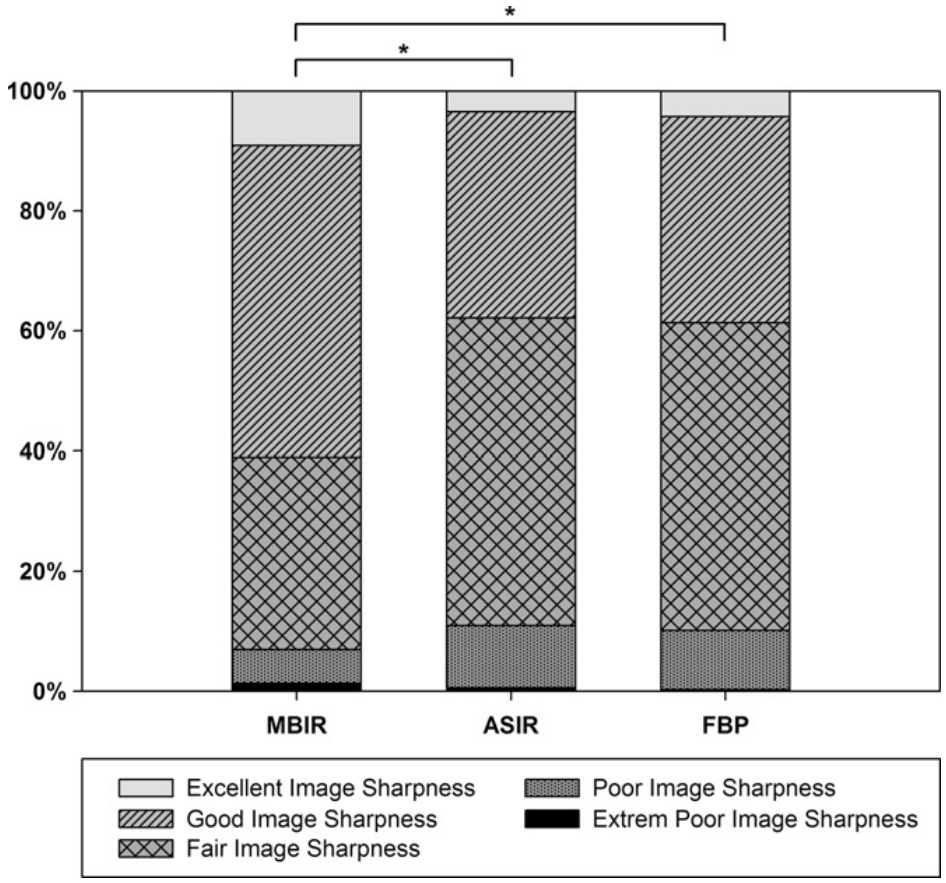

Figure 10 – Image sharpness as measured by qualitative scoring.

Image sharpness was significantly improved with MBIR as compared to ASIR (*p<0.001) and FBPR (*p<0.001); however, ASIR and FBPR were comparable (*p=0.61).

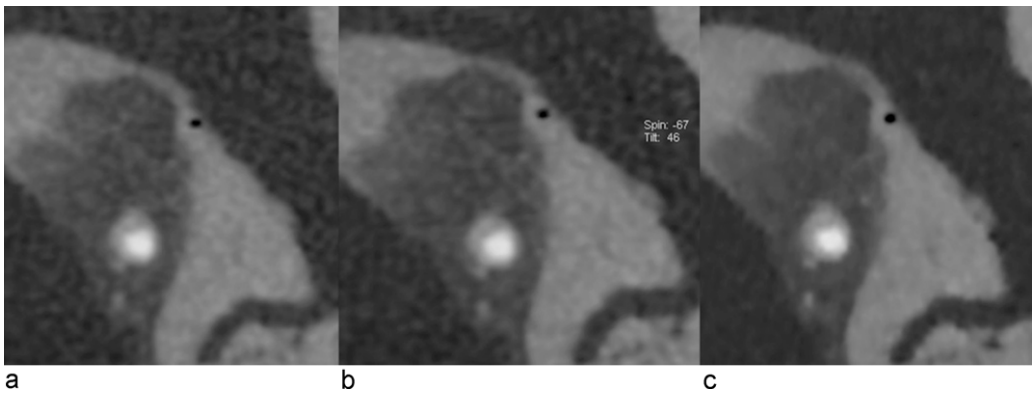

Figure 11 – Cross-sectional CT images of a non-calcified coronary plaque.

Images reconstructed with (a) FBPR, (b) ASIR, and (c) MBIR technique. Note the substantial reduction in noise resulting in improved sharpness of the vessel lumen and adjacent vessel wall (c) as compared to (a) and (b).

DOI:10.14753/SE.2015.1797

4.2.2 Quantitative image analysis

Inter- and intra-reader correlation coefficients ranged from 0.72 to 0.91 and 0.79 to 0.94, respectively, **Table 6**.

Table 6 – Inter- and intra-observer correlation for quantitative parameters.

	Inter-observer correlation	Intra-observer correlation
Luminal CT number	0.91	0.94
Image noise	0.82	0.79
CT number of adipose tissue	0.72	0.92

Mean luminal CT number was on average 6-10 HU higher in images reconstructed with MBIR than in those reconstructed with FBPR and ASIR ($p<0.05$, both; **Figure 12**).

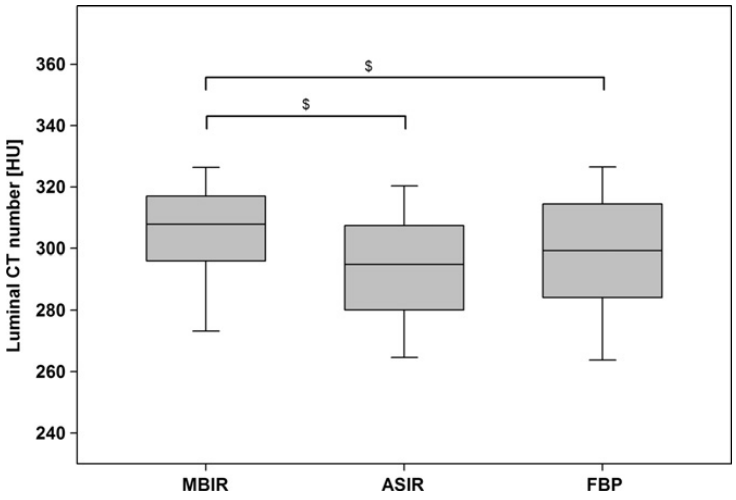

Figure 12 – Mean attenuation in the coronary arteries.
Mean luminal CT number was higher in images reconstructed with MBIR than in those reconstructed with FBPR and ASIR ($^{\$}p<0.05$, both).

Mean image noise was 16.0±5.1 HU in images reconstructed with FBPR, 14.5±4.3 HU in images reconstructed with ASIR, and 10.2±4.0 HU in images reconstructed with MBIR, **Figure 13**. Quantitative assessment of image noise correlated significantly with the qualitative image noise score ($r=0.43$, $p<0.001$).

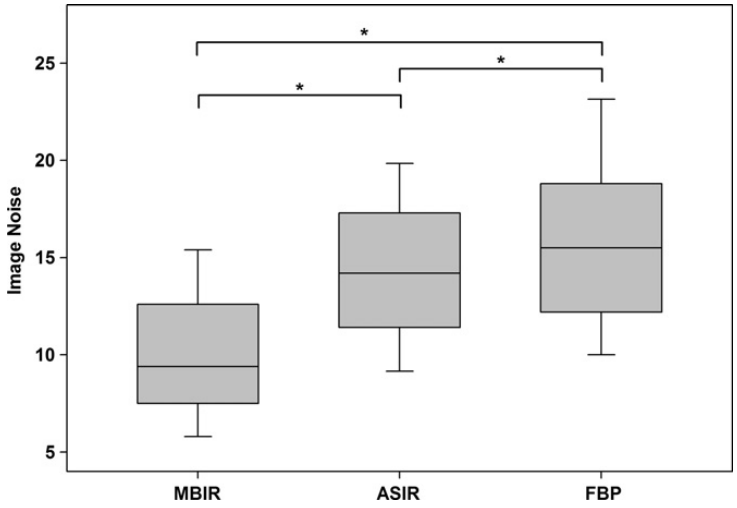

Figure 13 – Image noise as assessed by quantitative analysis.

The three reconstruction techniques were significantly different for image noise (*p<0.001).

Mean CNR was 26±9 HU in images reconstructed with FBPR, 29±15 HU in images reconstructed with ASIR, and 44±19 HU in images reconstructed with MBIR. The image noise and CNR among the three reconstruction techniques were significantly different (p<0.001, both). Image noise was highest using FBPR and lowest using MBIR (p<0.001, all); whereas CNR was lowest using FBPR and highest using MBIR (p < 0.001, all), see **Figure 14**. MBIR increased the CNR by 51-69% while decreasing the noise by 30-36% as compared to both other techniques of ASIR and FBPR.

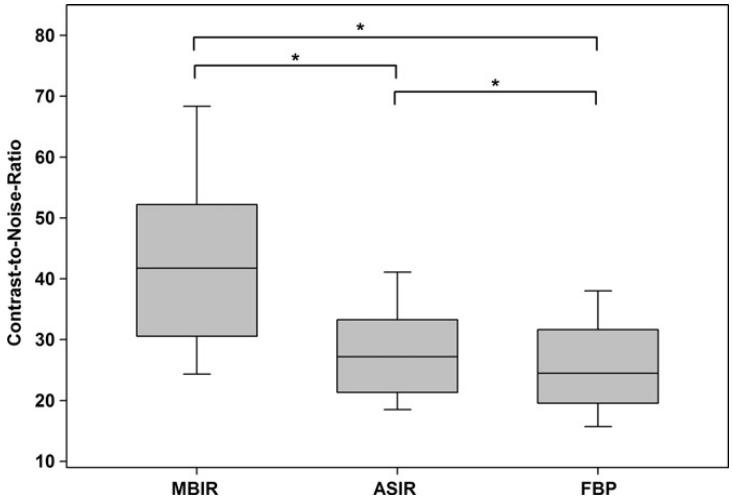

Figure 14 – Contrast-to-noise ratios in the coronary arteries.

The three reconstruction techniques were significantly different for CNR(*p<0.001).

DOI:10.14753/SE.2015.1797

4.3 Automated plaque assessment with coronary CTA and image reconstruction

A total of 2313 coronary CTA cross-sections with an increment of 0.5 mm were assessed from the proximal 40 mm of nine coronary arteries for this sub-study, each reconstructed with FBPR, ASIR and MBIR. Of those, data were co-registered and available in 2295 cross-sections (99.6%) resulting in 765 triplets of images. Average measured plaque area was 8.5±3.5 mm^2 with a plaque burden of 51.7±13.8%. Nearly two-third (59.5%) of the cross-sections contained no calcification, one-third moderate calcification (32.6%) and less than a tenth (7.9%) severe calcification. Examples for co-registered cross-sections and the differences in automatically fitted vessel-wall boundaries are illustrated in **Figure 15.** Further specimen characteristics are provided in **Table 7.**

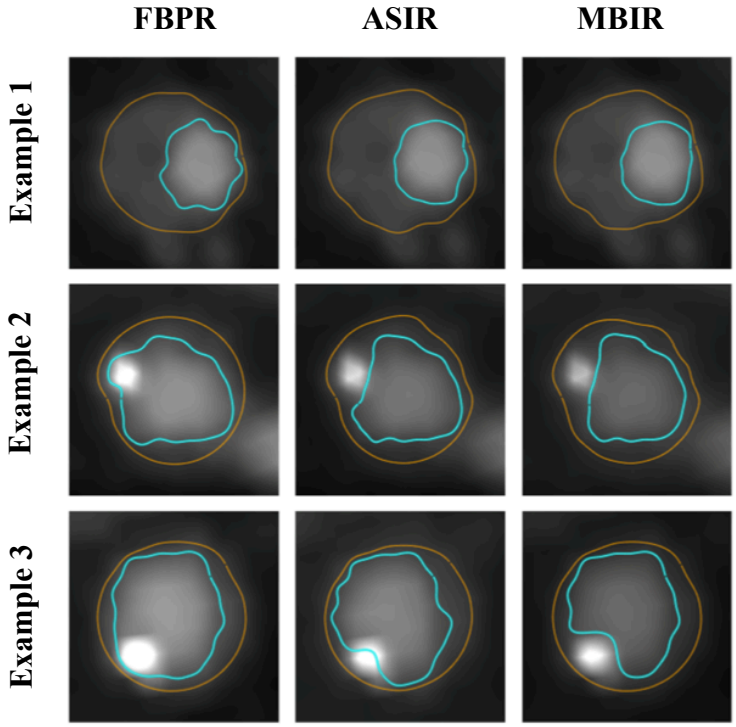

Figure 15 – Three examples of automatically fitted vessel-wall boundaries.

Example 1 demonstrates a cross-sectional image of the coronary artery with adjunct non-calcified plaque. No boundary correction was necessary in all three image reconstruction algorithms. *Example 2* shows the cross-section of a partially calcified coronary plaque. The automatically fitted inner vessel-wall boundary in FBPR did wrongly include the calcification within the lumen. *Example 3* shows the cross-section of a more calcified plaque than example 2. The automatically fitted inner vessel-wall boundary in FBPR but also in ASIR delineated the lumen incorrectly.

DOI:10.14753/SE.2015.1797

Table 7 – Study sample characteristics stratified by performance of any vessel-wall boundary corrections.

	Overall	Any boundary corrections	No boundary corrections	*p*-value
N	**2295**	**712**	**1583**	
Reconstruction Algorithm				<0.0001
FBPR	33.3% (765)	39.3% (280)	30.6% (485)	
ASIR	33.3% (765)	34.8% (248)	32.7% (517)	
MBIR	33.3% (765)	25.9% (184)	36.7% (581)	
Vessel Territory				0.98
LAD	37.9% (870)	37.9% (270)	37.9% (600)	
LCX	31.2% (717)	31.5% (224)	31.1% (493)	
RCA	30.9% (708)	30.6% (218)	31.0% (490)	
Calcification				<0.0001
No	59.5% (1366)	37.4% (266)	69.5% (1100)	
Moderate	32.6% (749)	44.5% (320)	27.1% (429)	
Severe	7.9% (180)	17.7% (126)	3.4% (54)	
Distance from ostium (mm)	22.1±13.1	22.7±13.2	21.8±12.9	0.11
Min. luminal diameter (mm)	2.7±0.8	2.6±0.8	2.7±0.9	0.001
Vessel Area (mm^2)	17.2±6.6	18.1±7.5	16.9±6.1	0.0002
Plaque Area (mm^2)	8.5±3.5	9.5±4.3	8.0±2.9	<0.0001
Plaque burden (%)	51.7±13.8	54±12.7	50.7±14.2	<0.0001

All continuous measurements with respect to coronary CTA were derived from corrected image datasets.

DOI:10.14753/SE.2015.1797

4.3.1 Feasibility of automatic vessel-wall delineation for plaque assessment

Any corrections of the outer or of the inner vessel-wall boundaries were performed in a total of 712 cross-sections (31.0%), while the outer vessel-wall boundary was corrected in 400 cross-sections (17.4%) and the inner in 381 cross-sections (16.6%). For both the outer and the inner vessel-wall, the boundary circumference was on average reduced by the manual corrections (delta of -0.6±1.8 mm for the outer, and delta of -0.9±1.1 mm for the inner vessel-wall comparing the boundary circumference before and after the manual corrections, both $p<0.0001$). The correction of one boundary (inner or outer) lasted on average for 21±4 seconds, for both boundaries 46±5 seconds. Corrections of vessel-wall boundaries were performed with a similar frequency for all three vessel territories ($p=0.98$), whereas more often performed at the side of moderate and severe calcification ($p<0.0001$), **Table 7**. The minimal luminal diameter was smaller whereas the cross-sectional vessel area and the plaque burden were larger in cross-sections with boundary corrections as compared to those without any corrections (all $p\leq0.001$, **Table 7**). No difference was observed regarding the distance from the ostium ($p=0.11$).

4.3.2 Impact of iterative reconstruction on automated vessel-wall delineation

Comparing the portion of cross-sections with boundary corrections (of the inner or/and the outer vessel-wall) between FBPR, ASIR, and MBIR, a stepwise reduction of corrected cross-sections was observed using MBIR as compared to ASIR and FBPR (26% and 34% relative reduction, respectively; all $p\leq0.0003$), **Table 7** and **Figure 16.** The difference between FBPR and ASIR was marginally non significant ($p=0.09$).

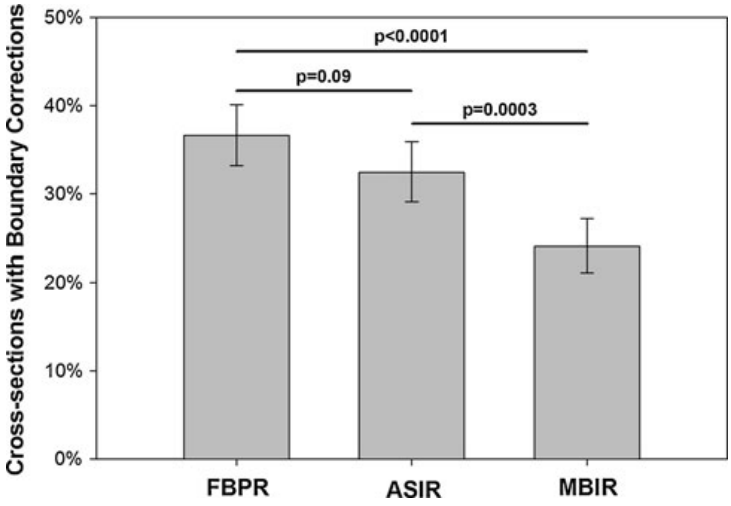

Figure 16 – Percentage of cross-sections with any boundary corrections stratified by image reconstruction algorithms.

A significant reduction of boundary corrections (to the inner or/and outer vessel-wall) was observed when MBIR was applied for image reconstruction as compared to ASIR or FBPR (all $p \leq 0.0003$).

Similarly, the percentage of cross-sections with inner vessel-wall boundary corrections was not different between FBPR and ASIR ($p=0.79$), while MBIR demonstrated again a smaller percentage of corrected cross-sections for the inner vessel- wall boundaries when compared to FBPR and ASIR (27% and 29% relative reduction, respectively; all $p \leq 0.009$), **Figure 17.**

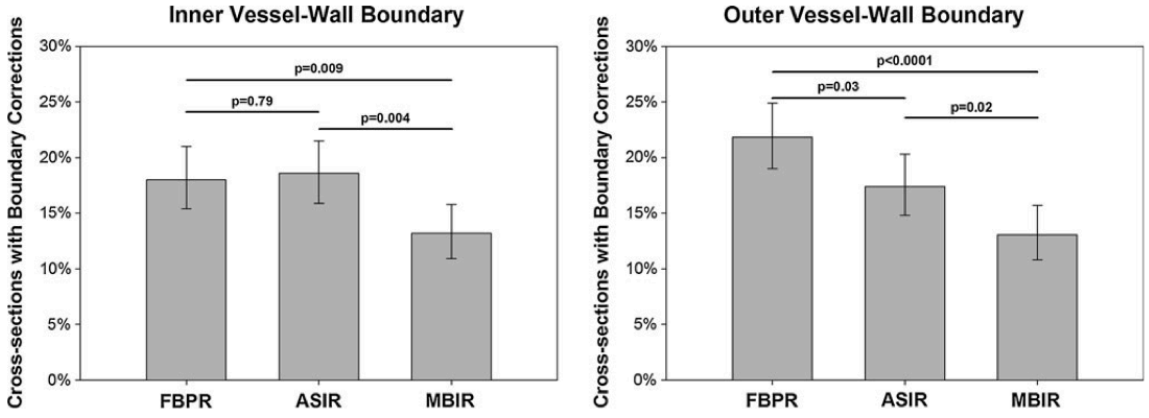

Figure 17 – Corrections of the outer and inner vessel-wall boundaries stratified by image reconstruction algorithms.

For both vessel-walls, MBIR led to a reduced need for boundary corrections as compared to ASIR or FBPR (all p≤0.02). Further, a reduction of outer vessel-wall boundary corrections were observed for ASIR as compared to FBPR (p=0.03).

For the outer vessel wall boundaries, the cross-sections with boundary corrections were reduced in ASIR as compared to FBPR and further reduced in MBIR (20% and 25% relative reduction, respectively; all p≤0.03), **Figure 17.** In cross-sections with any corrections, the degree of manual adjustments to the boundary circumference (in mm) did not differ between FBPR, ASIR, and MBIR (all p>0.64), **Figure 18.**

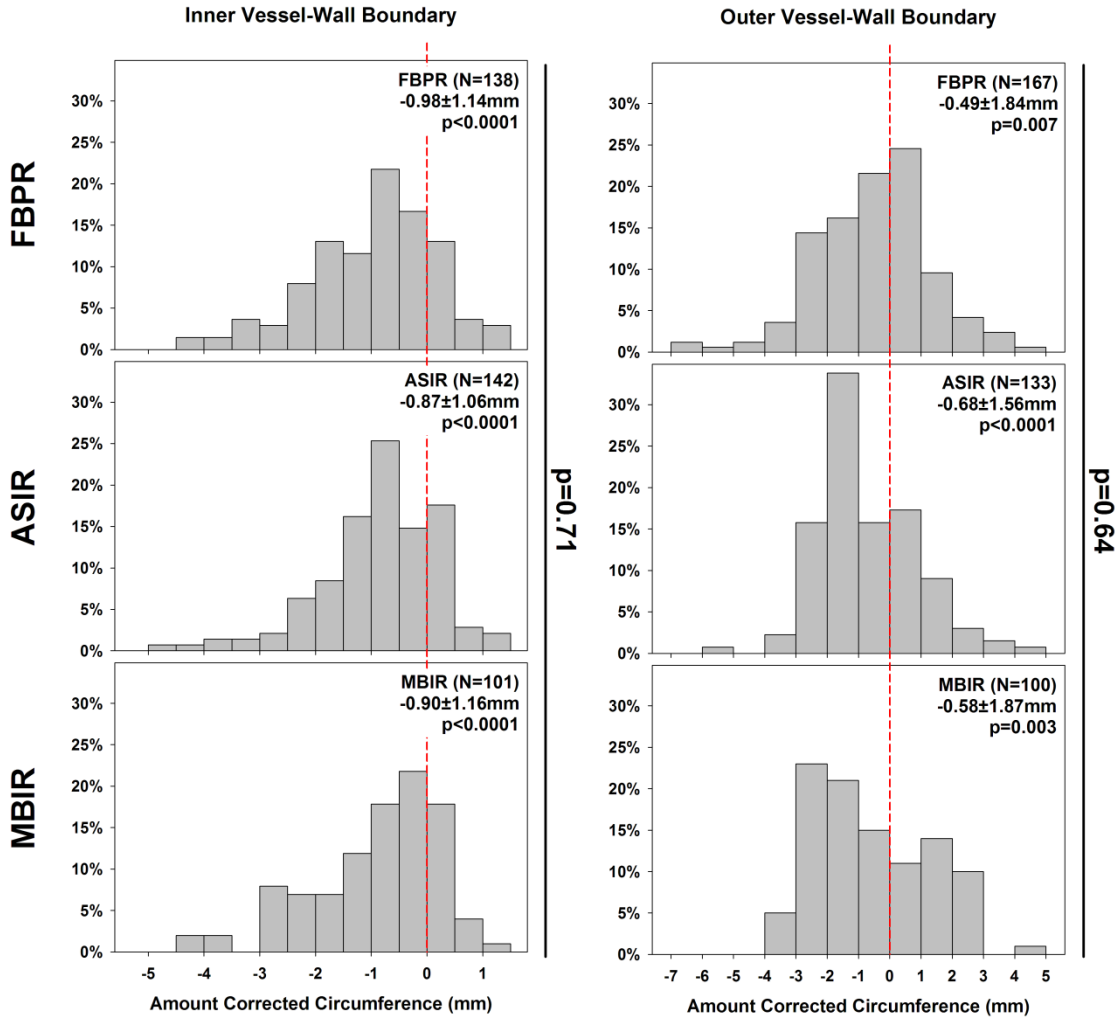

Figure 18 – Comparison of the corrected amount of the boundary circumference between image reconstruction algorithms.

All data demonstrated on average a significant reduction of the automatically fitted boundary circumference due to the manual corrections (all p≤0.003). However, no differences were observed regarding the corrected amount of boundary circumference between the image reconstruction algorithms (all p≥0.64).

On a per-vessel level, 32.5% (median, IQR: 27.5-48.1) of the entire assessed vessel length was corrected in FBPR, 29.2% (median, IQR: 23.8-43.0) in ASIR and 19.1% (median, IQR: 11.4-36.3) in MBIR. This resulted in a significant reduction of the corrected vessel length in MBIR as compared to ASIR and to FBPR (p=0.008 and p=0.004, respectively), while the difference between ASIR and FBPR was marginal (p=0.05), **Figure 19.**

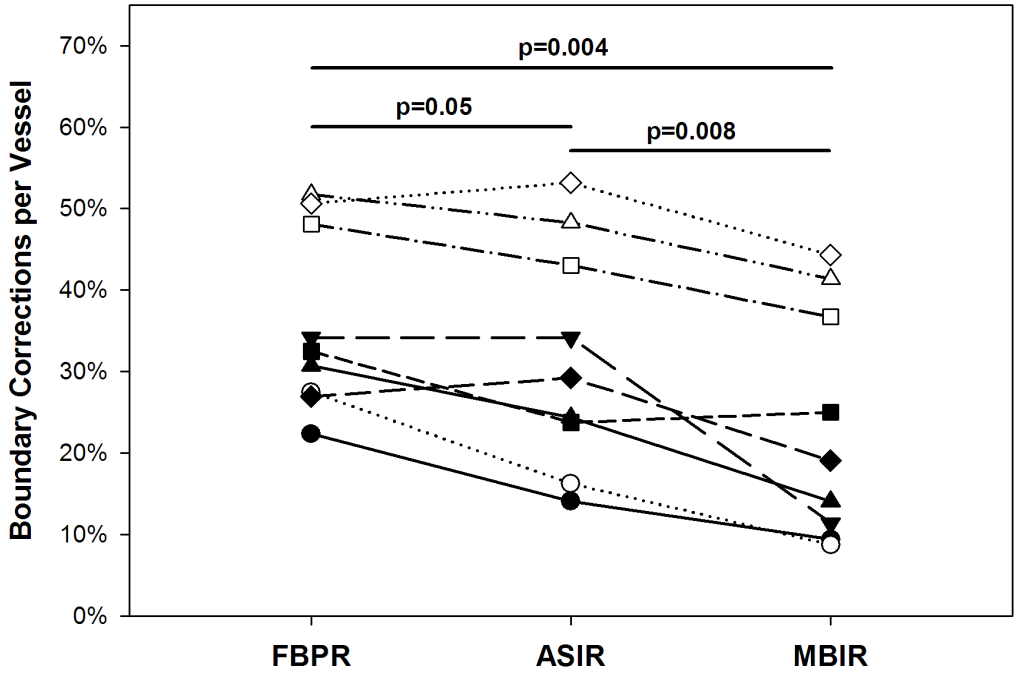

Figure 19 – Percentage of cross-sections with any boundary corrections per vessel stratified by image reconstruction algorithms.

Assessing the need for boundary corrections per vessel and comparing it between FBPR, ASIR and MBIR, a stepwise reduction was observed.

4.3.3 Regional agreement of vessel-wall boundary correction

On a per cross-section level of co-registered triplets (n=765), 53.6% required no corrections in any of the three image reconstruction algorithms. In contrast, 16.3% of the co-registered triplets were corrected in all three image reconstruction algorithms, **Figure 20.** Overall, there was a moderate agreement for performed corrections of the

vessel wall boundaries between all three image reconstruction algorithms (κ=0.53) and increased to good agreement if limited to FBPR and ASIR only (κ=0.61). Accordingly, no agreement existed in 30.1% between all three image reconstruction algorithms. Of those, nearly one third were cross-sections with vessel-wall boundary corrections in FBPR and ASIR, but not in MBIR, **Figure 20.**

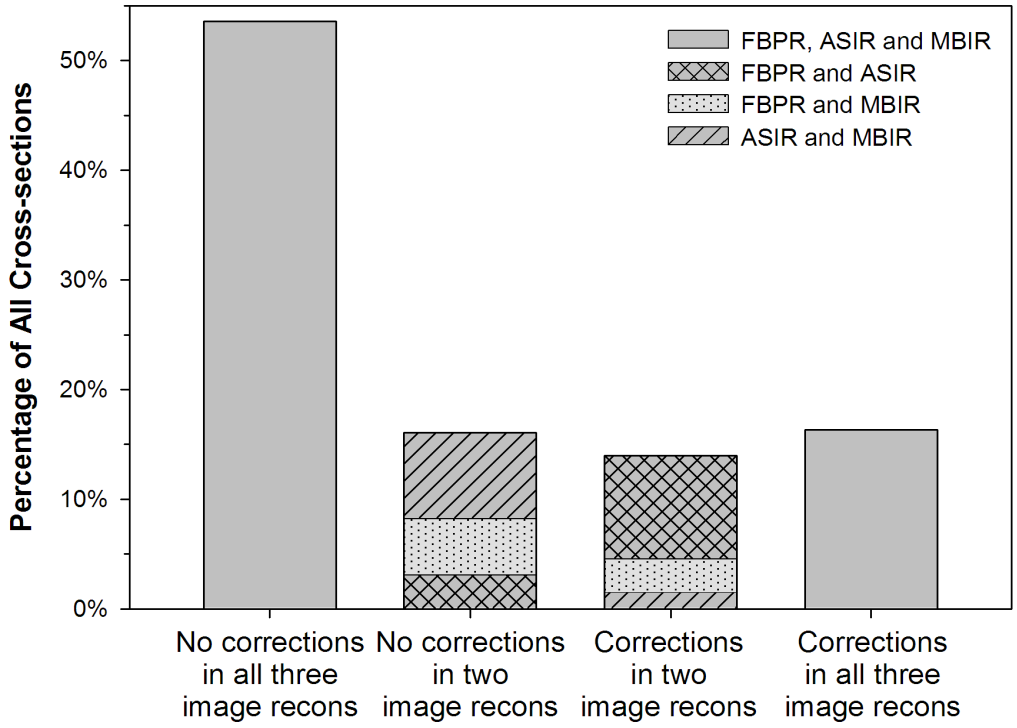

Figure 20 – Regional agreement for boundary corrections between FBPR, ASIR and MBIR.

Co-registered cross-sections were stratified according to the agreement (vessel-wall boundary corrections yes/no) in all three or in two out of three image reconstruction algorithms. In about 70%, agreement regarding the need for boundary corrections was achieved between all three image reconstruction algorithms, which resulted in an overall κ of 0.53.

DOI:10.14753/SE.2015.1797

4.3.4 Benefit of MBIR for automated vessel-wall delineation

Comparing the cross-sections where a benefit of MBIR was observed over FBPR (n=132) to those with no differences between MBIR and FBPR (n=597), only the extent of calcification was independently associated, **Table. 8.** The odds for the benefit of MBIR over FBPR increased by about 3-folds for the presence of moderate calcification [OR: 2.9 (95%CI: 1.9-4.5), p<0.0001], and by about 6-folds for the presence of severe calcification [OR: 5.7 (95%CI: 2.6-12.7), p<0.0001]. Minimal luminal diameter, plaque area and burden did not show any association with the benefit of MBIR over FBPR for the automated delineation of vessel-wall boundaries (all p≥0.45). A similar pattern was observed for the benefit of MBIR over ASIR, **Table 8.**

Table 8 – The association of plaque characteristics with the benefit of MBIR over FBPR (and over ASIR).

	OR (95%CI)	***p*-value**
Association to the benefit of MBIR over FBPR		
Calcification		
Moderate	2.9 (1.9-4.5)	<0.0001
Severe	5.7 (2.6-12.7)	<0.0001
Min. luminal diameter	1.3 (0.6-2.7)	0.48
Plaque Area	1.0 (0.9-1.1)	0.66
Plaque burden	1.0 (1.0-1.1)	0.44
Association to the benefit of MBIR over ASIR		
Calcification		
Moderate	4.3 (2.7-7.0)	<0.0001
Severe	9.2 (4.0-21.0)	<0.0001
Min. luminal diameter	0.7 (0.3-1.6)	0.49
Plaque Area	1.1 (1.0-1.3)	0.11
Plaque burden	1.0 (0.9-1.0)	0.37

DOI:10.14753/SE.2015.1797

4.3.5 Estimated time saving for automated plaque assessment

With an average time of 21 seconds for correcting one boundary per cross-section (inner or outer vessel-wall), and 45 seconds for correcting both boundaries per cross-section (inner and outer vessel-wall), the usage of MBIR would reduce the assessment time for an average heart (including the proximal 40 mm of all three coronary arteries) by an average of 9 minutes as compared to ASIR and 12 minutes as compared to FBPR. The time benefit of using MBIR as compared to FBPR increased to 18 and 24 minutes per heart if a vessel-length of 60 and 80 mm would have been automatically assessed (**Figure 21**).

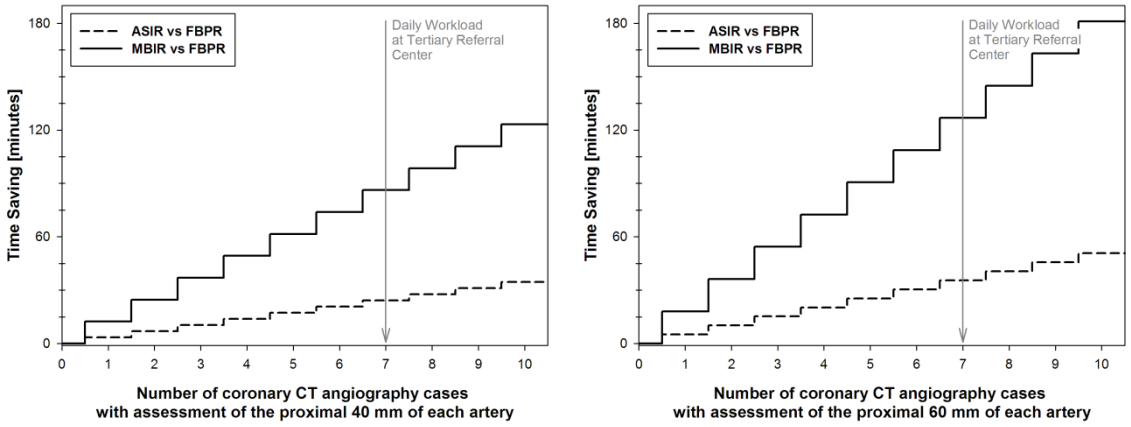

Figure 21 – Estimated time saving for automated plaque assessment using iterative reconstruction algorithms.

Based on the study results, the use of MBIR would reduce the assessment time by an average of 12 minutes (or 18 minutes) as compared to FBPR for an average coronary CT angiography case where the proximal 40 mm (or 60 mm) of all three coronary arteries were assessed.

DOI:10.14753/SE.2015.1797

4.4 Characterization and classification of atherosclerotic plaque with MRI

59 plaque cross-sections could be co-registered with corresponding high-field MRI datasets (T1, T2, UTE). All sections had evidence of atherosclerotic disease with calcification present in 48% (28/59) and lipid-rich necrotic core in 56% (33/59). We used 31 co-registered sections to study plaque characteristics and 28 were used for the analysis.

The image quality of the UTE images was high, averaging 4.1±0.7, and was diagnostic in all cases. MRI had an excellent sensitivity (100%), specificity (90%) and both positive (80%) and negative (100%) predictive values for the identification of calcium, **Table 9**. The sensitivity, specificity, positive and negative predictive values for lipid-rich necrotic core recognition with MRI were 90%, 75%, 90% and 75%, respectively, **Table 9**. MRI failed to identify lipid-rich necrotic areas in two plaques; however, both these lesions were classified histologically as early lesions with only very small lipid-rich necrotic cores. **Table 10** shows the comparison of plaque classification by MRI and histology. Complete agreement was seen in 22/28 cases. Type I-II lesions were identified correctly by MRI in all cases. Two sections with Type III plaques by histology were misclassified by MRI as having small lipid-rich necrotic cores. It should be noted that prior to the consensus discussion, 2/3 readers had classified these plaques as Type III by MRI as well. Among Type IV-V lesions, 2 plaques were falsely classified as calcified by MRI. Overall only 6/28 lesions were misclassified by MRI, resulting in a good correlation between MRI and histology (κ value of 0.69). Excellent inter-observer agreement was found for the detection of plaque components (calcification and lipid-rich necrotic core) by MRI with a κ value of 0.80 and 0.82, respectively ($p<0.0001$). The inter-observer correlation for overall MRI plaque classification was also high ($\kappa=0.78$, $p<0.0001$).

Examples for plaque classification are shown in **Figure 22-25.**

DOI:10.14753/SE.2015.1797

Table 9 – Detection of calcification and lipid-rich necrotic core with MRI.

Calcification			
	Ca on Histology	**No Ca on Histology**	**n**
Ca on MRI	8	2	10
No Ca on MRI	0	18	18
n	8	20	28
Sensitivity: 8/8 = 100% (95%CI, 63-100%)		PPV: 8/10 = 80% (95%CI, 44-98%)	
Specificity: 18/20 = 90% (95%CI, 68-99%)		NPV: 18/18 = 100% (95%CI, 82-100%)	
Lipid-rich Necrotic Core			
	LRNC on Histology	**No LRNC on Histology**	**n**
LRNC on MRI	18	2	20
No LRNC on MRI	2	6	8
n	20	8	28
Sensitivity: 18/20 = 90% (95%CI, 68-99%)		PPV: 18/20 = 90% (95%CI, 68-99%)	
Specificity: 6/8 = 75% (95%CI, 35-97%)		NPV: 6/8 = 75% (95%CI, 35-97%)	

DOI:10.14753/SE.2015.1797

Table 10 – Classification of coronary plaques by MRI vs. histology.

		Histology				
		Type I-II	Type III	Type IV-V (A)	Type IV-V (B)	Total
MRI	Type I-II	2	…	…	…	2
	Type III		4	…	…	4
	Type IV-V (A)	…	2	9	…	11
	Type IV-V (B)	…	…	2	7	9
	Type VIII (A)	…	…	1	…	1
	Type VIII (B)	…	…	…	1	1
	Total	2	6	12	8	28

DOI:10.14753/SE.2015.1797

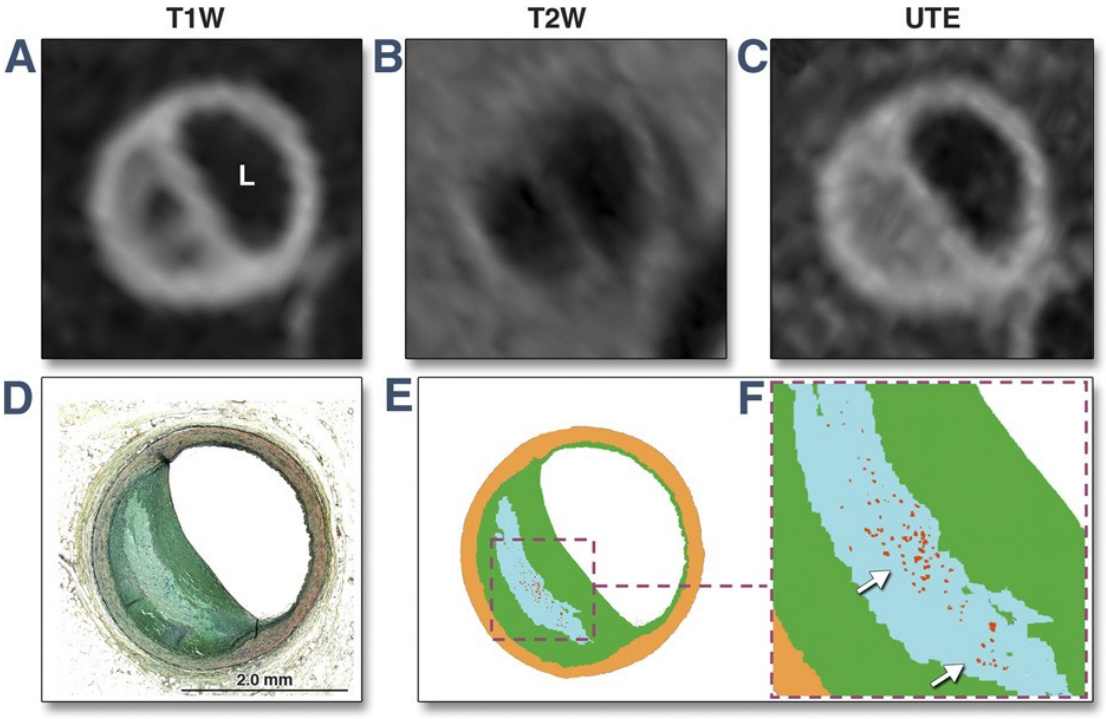

Figure 22 – T1, T2 and UTE images of a partially calcified lipid-rich necrotic plaque.

T1-weighting (A) reveals a large plaque with two focal areas of profound hypointensity. These areas are also hypointense on the T2-weighted image (B) but are isointense on the UTE image (C), consistent with foci of calcification. Profound hypointensity is seen in the plaque on the T2-weighted image (B), consistent with a lipid-rich necrotic core. Pentachrome staining of the plaque cross-section (D) correlates extremely well with the MRI. Segmentation of the histological section (E, F) shows the lipid-rich necrotic core (light blue) and the foci of calcification (red dots, white arrows). The plaque was correctly classified as a Type IV-VB lesion by MRI. L= Lumen.

DOI:10.14753/SE.2015.1797

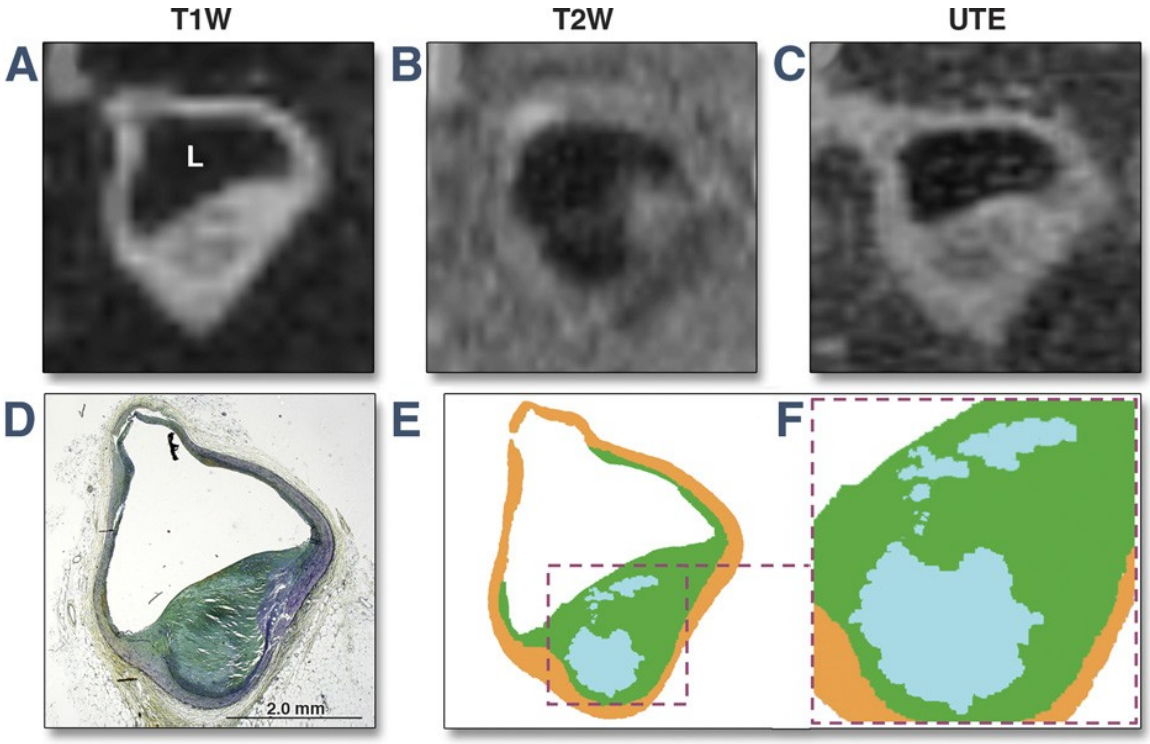

Figure 23 – A coronary artery plaque with a non-calcified lipid-rich necrotic core.

No profound areas of hypointensity are seen on the T1-weighted image of the plaque (A), excluding plaque calcification. The plaque interior, however, is hypointense on the T2 image (B), consistent with a lipid-rich necrotic core. Plaque histology (D) and segmentation (E, F) correlated well with the MRI and revealed the LRNC (light blue). The plaque was correctly classified as a Type IV-VA lesion by MRI. L= Lumen.

DOI:10.14753/SE.2015.1797

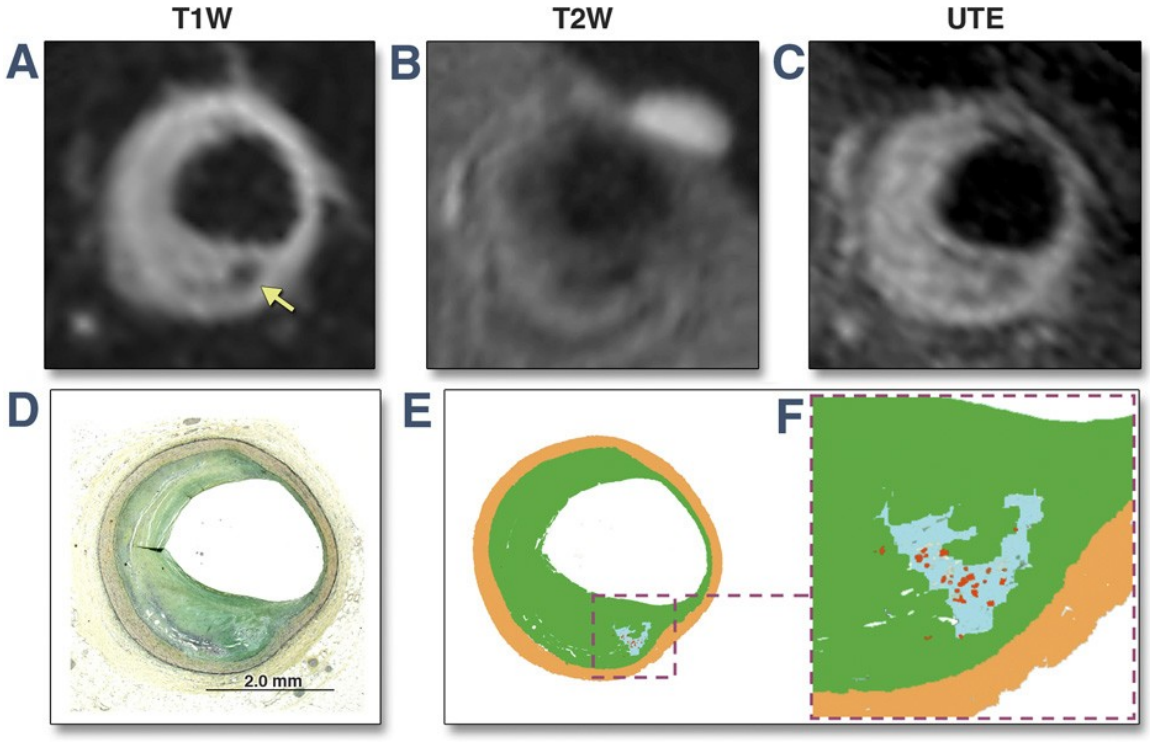

Figure 24 – Example of plaque misclassification by MRI.

Profound signal hypointensity (arrow) is seen on the T1-weighted image (A) with corresponding recovery of signal in the UTE sequence (C). A corresponding small-localized area of hypointensity is seen on the T2-weighted image (B), which could be due either to an isolated focus of calcification or due to calcification of a small lipid-rich necrotic core. (D-F) Histology revealed that the hypointense focus is produced by diffuse calcification (red dots) of a small lipid-rich necrotic core (light blue). The plaque was incorrectly classified by MRI as VIIIB (fibrocalcific without a lipid-rich necrotic core). Only 2/20 lipid-rich necrotic cores were missed by MRI in the study, both of which were small and focal (see panels D, E).

DOI:10.14753/SE.2015.1797

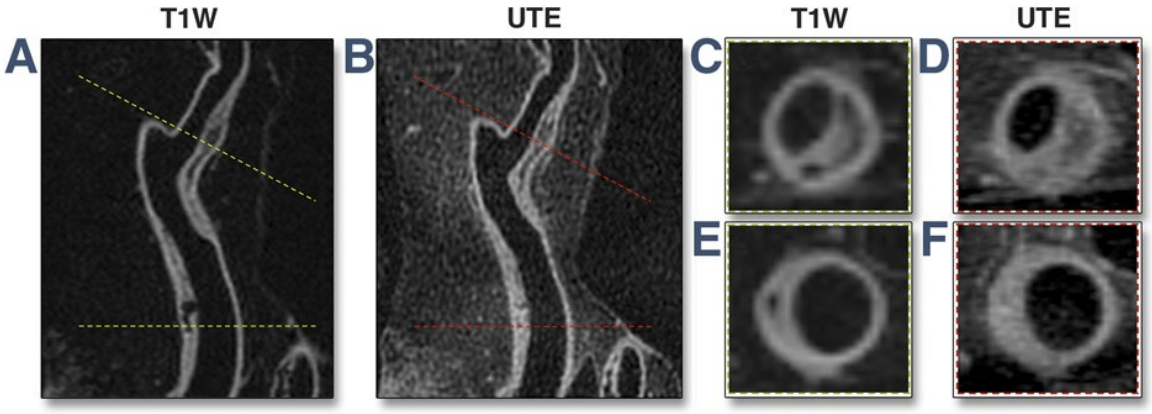

Figure 25 – T1 and UTE multiplanar reformats (MPRs) of the left anterior descending coronary artery.

T1-weighted (A) and UTE (B) MPRs of the LAD show two large plaques on opposite sides of the vessel wall. Cross-sectional images through these plaques are shown with T1 (C, E) and UTE (D, F). In both plaques, but in particular in the lower one (A, B, E, F), areas of profound signal hypointensity are seen on T1 images, but not on the UTE images, consistent with foci of plaque calcification.

DOI:10.14753/SE.2015.1797

5 Discussion

5.1 Coronary plaque visualization with CT angiography

5.1.1 Histopathological correlates of the napkin-ring sign

In the search to find a pattern of coronary atherosclerotic plaque in coronary CT angiography beyond CT attenuation that is associated with advanced coronary atherosclerotic plaque several authors have described the napkin-ring sign (43,44,46). However, the factors that influence the delineation of this sign remain unclear. In this *ex vivo* study we used the gold standard histopathology to define the equivalent of the NRS and the components of atherosclerotic plaque that correspond to this sign in coronary CT angiography. Our results demonstrate that the histopathological equivalent of the NRS is a large and advanced atherosclerotic lesion with a large necrotic core.

Plaques with low density values (typically below 30HU) in coronary CT angiography correlate with lipid-rich plaques as detected in IVUS or OCT (43,83). There is also evidence, that culprit lesions in acute coronary syndrome show lower density values than non-culprit lesions (84). However, due to partial volume effects, the density values show a large variability preventing a reliable differentiation of plaque types and detection of lipid-rich plaques based solely on HU values (85). Therefore markers of atherosclerotic plaques beyond attenuation are needed for plaque stratification in coronary CTA. Recently, a number of studies have reported a hypodense central plaque portion surrounded by a hyperdense ring, consistent with the NRS, in patients with ACS. In the present study, the density values of the rim were significantly higher than the density measured in the center of the lesion. In a report by Pflederer et al., a similar ring like pattern was found in 25% of culprit lesions in patients presenting with ACS but never in patients presenting with stable angina (44). Kashiwagi et al. divided culprit lesions in patients with ACS in thin-cap fibroatheromas and non-TCFA plaques according to findings in optical coherence tomography. A ring-like pattern was found in 44% of TCFAs but only in 4% of plaques without a thin fibrous cap (43). Nishio et al.

found a ring-like pattern in 44% of disrupted plaques detected by angioscopy in patients with suspected ischemic heart disease, but only in 6% of plaques without signs of rupture (46). In the present study the most distinct histopathologic feature of plaques exhibiting the NRS in CT and the strongest independent predictor was the presence of a large necrotic core representing the center of the napkin-ring sign. In plaques with positive NRS, the necrotic core was more than twice as large as in plaques without the NRS (1.1 mm^2 vs. 0.5 mm^2; respectively). Invasive studies using IVUS and OCT showed that the size of the necrotic core in coronary atherosclerosis correlates with the risk for plaque rupture (8,86). These findings have been confirmed by histopathology. Virmani et al. have reported in a series of 400 patients who died of sudden coronary death 80% of ruptured plaques had a necrotic core area of >1 mm^2 (6).

The second most important feature in plaques with an NRS in CT was the size of the plaque surrounding the necrotic core, which was also nearly twice as large compared to plaques without the NRS (10.2 mm^2 vs. 6.4 mm^2, $p<0.001$). The plaque component surrounding the necrotic core mainly consists of fibrous tissue and smooth muscle cells (87) and represents the equivalent of the rim of the napkin-ring sign as seen in CT.

The association between plaque size and NRS is explained in that the limited spatial resolution of CT requires a certain number of voxels representing a specific plaque component in order to be able to differentiate them from each other, i.e. the hypodense core from the hyperdense rim. While a large plaque area is required for the delineation of the napkin-ring sign, it is also a feature of advanced atherosclerotic plaques. Several CT and IVUS studies have reported that unstable lesions associated with ACS show a larger plaque area with positive remodeling compared to stable lesions in patients with stable angina (17,18,88). The association of a large plaque area with the NRS is also mirrored in the association of NRS and plaque burden and the fact that the napkin-ring sign was more commonly detected in proximal segments of the coronary artery tree.

Initially it was speculated that the ring like sign was caused by deep calcifications within the plaque. Indeed, spotty calcifications were slightly more common in plaques where the NRS was present (42% vs. 29%). However, the formation of these calcifications did not explain the appearance of the NRS. In addition, several authors demonstrated the absence of macrocalcifications around the hypodense central part of

the napkin-ring sign in non-enhanced CT scans (45).

Consequently, most authors support the hypothesis that the napkin-ring sign is caused by vasa vasorum enhancing the outer curvature of the plaque. Our results demonstrate that angiogenesis is associated with the NRS (48%) but it is also quite common in plaques not characterized by an NRS (30%). In our ex-vivo study, the contrast material injected in the coronary arteries had high viscosity due to the use of methylcellulose and probably did not enter the vasa vasorum. Thus, we believe that the contrast agent did not enhance the outer rim of the plaque. This is in line with previous reports demonstrating the NRS in non-contrast enhanced images (45). However, it is conceivable that neovascularization contributes to the delineation of the napkin-ring sign in-vivo by increasing the attenuation of the tissue around the core after the administration of contrast media. Independent of this, the fact that neovessels are often found in plaques with an NRS is important as neovascularization arising from adventitial vasa vasorum is common in advanced coronary atherosclerotic lesions and has been associated with intraplaque hemorrhage and subsequent plaque destabilization (89,90).

Somewhat surprisingly, we found microcalcifications in the rim surrounding the core only in a quarter of NRS plaques (27%). Microcalcifications have also been suggested as a possible cause for an increase in CT attenuation as in some cases the brighter rim of the NRS has been observed in non-contrast scans (45). Indeed, data from atherosclerosis models shows that microcalcifications often develop around the necrotic core (91). In the present study, microcalcifications were more commonly found in plaques without an NRS (46%), suggesting that microcalcifications can elevate the Hounsfield values of the tissue around necrotic core and thus lead to volume averaging which might prevent the smaller hypodense cores from being identified in coronary CT angiography. The presence of microcalcifications around the core might also explain why density values in advanced atherosclerotic plaques vary, making a reliable differentiation of plaques types difficult with CT (85).

DOI:10.14753/SE.2015.1797

5.1.2 Coronary plaque visualization with FBPR, ASIR, and MBIR technique

Our study demonstrates better image quality using MBIR compared with ASIR or FBPR for both qualitative and quantitative image analysis. Analysis of ASIR and FBPR yielded similar image quality. The image noise was highest using FBP and lowest using MBIR; whereas CNR was lowest using FBPR and highest using MBIR. The described MBIR algorithm shows improved image sharpness as compared to ASIR and FBPR, but no differences were discovered among the three reconstruction techniques regarding the detection of calcifications. Qualitative image analysis revealed higher mean luminal CT numbers on average in images reconstructed with MBIR than in those reconstructed with FBPR and ASIR. The subjective image quality rating for MBIR was better than ASIR and FBPR images.

Previous studies that evaluated the image quality of iterative reconstructions in chest (51,92) and abdominal (50) CT demonstrated similar results for the comparison of ASIR with FBPR. In contrast to their experiences, we were not able to show significant difference regarding the image quality between ASIR and FBPR, that was rated equally. This might be related to the use of a subjective overall image quality scoring system. Interestingly Prakash et al. (51) have also found no difference for ASIR and FBPR for evaluation of small bronchioles of the lungs. Any difference was only present when an ASIR-HD reconstruction technique was used. The qualitative rating of image sharpness showed MBIR better than ASIR and FBPR images, however, ASIR and FBPR were not different. This finding is in line with the findings from overall image quality reading showing no differences between ASIR and FBPR but for MBIR. Coronary image sharpness was assessed subjectively with a considerable inter-observer variability. However, other studies assessing IQ have used similar scoring systems (76,77).

According to our results MBIR and ASIR were not more effective in the suppression of blooming artifacts than FBPR at constant X-ray tube settings. We hypothesized, that iterative reconstruction techniques would substantially lower blooming artifacts, enabling better appreciation of the vessel lumen, which have traditionally been recognized as limitation of cardiac CT. However, independent of the CT image

reconstruction technique, image quality was significantly worse when calcification was present.

The quantitative analysis showed lower image noise using MBIR as compared to ASIR or FBPR. We were unable to compare results of our study owing to lack of published clinical studies of the MBIR technique. However, prior phantom studies using the MBIR techniques for CT image reconstruction have reported potential for image noise and artifact reduction (52,73,93). Thus, lower image noise with MBIR and ASIR reconstruction techniques allow the use of sharper or greater edge-enhancement kernels, which may have contributed to the improved CNR ratio and aided in the visualization of small structures not satisfactorily evaluable with the more noise-prone filtered backprojection technique. That ability of ASIR technique to lower the image noise has already been found in several other non-coronary CT studies (50,51,53,92,94). Furthermore, an increase in CNR as in our study was also shown by an abdominal CT study evaluating the potential radiation dose reductions potentially related with this technique (50). The finding of lower noise and higher CNR together with better vessel sharpness using MBIR compared with ASIR or FBPR analysis may have an important clinical implication for the evaluation of coronary artery plaques that needs to be validated *in vivo*. Qualitative image analysis revealed higher mean luminal CT numbers on average in images reconstructed with MBIR than in those reconstructed with FBPR and ASIR. This can be explained by a narrower point spread function.

5.1.3 Effect of image reconstruction technique on automated plaque detection

Although several studies showed a good performance of automated coronary CTA assessment tools when compared with gold-standard, such as IVUS (48,78), the main drawback which precludes the wider clinical applicability of these tools is the need for significant corrections of the automatically fitted vessel-wall boundaries (42).

We demonstrated that with the use of MBIR for coronary CTA image reconstruction, the percentage of necessary corrections to the vessel-wall boundaries was significantly reduced when compared to ASIR and even more to FBPR. The need for boundary

corrections showed a high reproducibility and a regional agreement between FBPR, ASIR and MBIR. The benefit of MBIR over the other reconstruction algorithms was associated with the extent of calcification.

The use of iterative reconstruction algorithms, especially MBIR, improves the feasibility of automated coronary CTA assessment and may lead to a wider acceptance of plaque quantification and characterization in the daily clinical practice. Prior studies yielded multiple benefits of iterative reconstruction algorithms over FBPR. These include a reduction of image noise and an increase in the contrast to noise ratio, both closely linked to the observed improvement in image quality (95-97). This was achieved by incorporating noise statistical information of raw projection data and measuring electric noise (71). Accordingly, novel coronary CTA scan protocols have been developed which allow clinical scanning at much lower radiation doses without impeding the image quality as compared to FBPR (98,99). The results of our study are in line with these previous observations as the increased feasibility of automated plaque assessment using iterative reconstruction algorithms can be related to the improved image quality (78,100).

Another important benefit of iterative reconstruction algorithms is the reduction of blooming artifacts caused by calcification (101). Similarly, the blooming artifact at the site of metal objects, e.g. coronary stents is reduced if iterative image reconstruction algorithms are applied. In two clinical studies, it has been shown that the visualization and the evaluation of implanted coronary stents were more accurate when hybrid iterative reconstruction algorithms were applied (one study used SAFIRE [sinogram affirmed iterative reconstruction], one used ASIR), as compared to FBPR, even with lower radiation doses (102,103). In accordance, we observed a significant benefit of MBIR over FBPR at the sites of moderate, and even more, at the sites of severe calcifications, which resulted in more accurate automated delineation of vessel-wall boundaries. Particularly, MBIR helps to improve image quality ‘locally’ with respect to noise and resolution through several, iterative comparison between measurements and reconstructed image including data from statistical, but also system optics modeling (72).

Interestingly, assessing the influence of reconstruction algorithms on the accuracy of plaque burden measurements by coronary CTA as compared to IVUS, no difference was observed by Stolzmann et al. who used pure manual boundary delineation method (104). We did not assess the accuracy of coronary CTA in this study, however we observed a clear benefit of MBIR and a marginal benefit of ASIR over FBPR with respect to the feasibility of automated plaque assessment. Manual vessel-wall boundary delineation by experienced CT readers, as done in the study of Stolzmann et al. (104), is less dependent on image quality and blooming artifacts since the CT reader is trained to overcome those situations. On the other hand good image quality and reduced artifacts seem to have an incremental importance when using an automated plaque assessment.

The implementations of our findings may have significant aspects on everyday clinical practice. For coronary CTA, automated plaque assessment has shown to be accurate and less dependent on the readers' experience (42,48,49,78). Furthermore, the quantification of plaque volume is a strong prognostic marker (105) and the characterization of local lesions can determine their vulnerability (106). However, these data are rarely retrieved from coronary CTA in clinical practice due to the labor-intensive manual adjustments required by the currently used automated assessment tools. With the implementation of the iterative reconstruction algorithms, such as MBIR, in the routine clinical practice, automatically fitted vessel-wall boundaries must be corrected less frequently and the coronary CTA assessment time will be significantly reduced as compared to FBPR**.** This warrants a more systematical use of automated assessment tools for plaque quantification and characterization, since both have great potential to improve patients' management and long-term risk stratification.

5.2 Coronary plaque assesment with MRI

The utility of cardiac MRI in the classification of human coronary atherosclerotic plaque remains poorly defined. Moreover, coronary atherosclerotic plaques frequently calcify and any MRI classification scheme must therefore be able to reliably detect plaque calcification. Here we showed that a combination of T1, T2 and UTE MRI can robustly classify human coronary atherosclerotic plaques, including lipid-rich and

calcified lesions. We show that plaque classification with this approach correlates very strongly with plaque classification by histology. To the best of our knowledge, this is the first use of a UTE-based triple-contrast approach (T1, T2, UTE) in the evaluation of human coronary atherosclerosis.

Histological and invasive studies have shown that the majority of acute coronary syndromes result from rupture of advanced atherosclerotic plaques (4-6). These plaques typically have a large lipid-rich necrotic core covered by a thin fibrous cap (5). The histological threshold used to define a thin-cap is 65 μm (5), and is beyond the resolution of all non-invasive imaging techniques. Nevertheless, we show that MRI can accurately differentiate fibrous coronary plaques with no necrotic cores from those containing large lipid-rich necrotic cores. The role of calcification in plaque vulnerability remains unclear. While some have suggested that heavily calcified plaques are more stable (107,108), this is disputed by others (109,110). Regardless, accurate detection of calcification is vital for reliable plaque classification and is made possible by the addition UTE MRI.

The use of MRI is well established in the carotid arteries, and several studies have shown its strong correlation with histological analysis of endarterectomy specimens (55,56). The discrimination of lipid-rich necrotic cores in carotid arteries was originally described using T1, T2 and Proton Density (PD) weighted fast spin echo sequences with fat suppression. These studies report the delineation of lipid-rich necrotic core with a sensitivity of 90% and specificity of 65-74% (55,56). The use of UTE imaging in the carotid arteries *ex vivo* has also recently been described (60,61). While the experience in the carotid vascular bed is extremely valuable, a direct correlation with plaque morphology in the coronary arteries cannot be assumed. Direct imaging of plaque morphology with MRI in the coronary arteries is thus required to characterize the disease. The results of our study show that the classification of atherosclerotic plaque using MRI produces similar accuracy in the coronary and carotid arteries. Moreover, the incorporation of UTE MRI in our study resulted in a higher specificity for necrotic core detection compared to some of the prior carotid imaging studies (55,56). Several sequences, routinely performed during *in vivo* MRI of the carotids, could not be performed in this *ex vivo* study. The intravenous injection of gadolinium-based contrast agents in the carotid artery can delineate plaque neovascularization and fibrous cap

rupture, but could not be performed in our setting (58,111). Although some of the plaques in our study showed features suggesting surface disruption, the accuracy of this finding in fixed *ex vivo* coronary arteries remains unknown. We chose therefore to limit our classification to the plaque interior, where fixation has been shown not to have an effect on plaque characterization by MRI (112). Intra-plaque hemorrhage produces signal hyperintensity on T1 and off-resonance MRI images (113,114), and signal hypointensity in T2* weighted images (115,116). Plaque hemorrhage can thus be expected to produce marked hyperintensity on UTE images, in which the R2* effects are completely eliminated. No plaques with hemorrhage, however, were encountered in this study and this will need to be further tested in future studies.

Calcified tissues are rigid and hence have extremely short transverse relaxation times (significantly less than 1 ms). Conventional imaging sequences have echo times (TE) greater than 1 ms and are thus unable to detect any signal from the tissues. UTE MRI, however, has a TE in the low microsecond range, and has been used to image bones and carotid plaque calcification (60,61,117). The utilization of UTE imaging in the carotids yielded a sensitivity of 71% and specificity of 96% for the detection of calcium (60). UTE MRI, however, has not been used prior to this in the coronary arteries.

In vivo MRI of the coronary wall has been limited to date to the detection of wall thickening, delayed enhancement and intra-plaque hemorrhage (113,118,119). High-resolution *ex vivo* imaging of the coronary artery wall has been performed but on a very limited scale (68,112). Itskovich et al imaged *ex vivo* coronary plaques at 9.4T and used cluster analysis to successfully classify atherosclerotic plaques (68). UTE MRI, however, could not be performed in this study and limited the discrimination of plaque calcification (68). In contrast, the use of UTE MRI in our study allowed plaques with calcified components to be accurately classified. Moreover, we were able to reach higher inter-observer agreement for coronary plaque classification with our technique, than others have reported using T1, T2, PD, and 3D TOF imaging in the carotids (120).

Several factors underline the high image quality obtained in this study. The field strength used allowed high spatial resolution to be achieved without the loss of signal to noise ratio (SNR). The performance of our approach at lower field strengths (1.5-3T) will require further study. It should be noted, however, that the relative relaxation rates

of plaque components do not change at these fields. The exception to this is intraplaque hemorrhage, which is significantly easier to detect with T1 and UTE MRI at 1.5-3T because the longitudinal relaxivity (r1) of iron drops dramatically at higher fields. All the sequences described here can be performed with advanced cardiorespiratory gating and motion compensation. Translation of our approach on current clinical systems is thus feasible.

Several ongoing technical developments have the potential to further improve MRI of the coronary wall. Cardiac MRI in humans is being performed at 7T by several groups, but is complicated by specific absorption rate (SAR) limits and magnetic field inhomogeneity (63,67,121). Nevertheless, *in vivo* MRI of the coronary arteries has been performed at 7T in normal volunteers (63,67,121). Transmit arrays for B1 shimming over the heart at 7T have been developed and raise the possibility of selective inner volume excitation of the coronary segment of interest (121). While very preliminary, these data collectively raise the promise of 7T coronary wall imaging in the near future. Receive coils, optimized specifically for coronary wall imaging, as well as better motion correction algorithms will also need to be developed. Highly accelerated cardiac imaging using 128 element arrays is already feasible and could significantly reduce motion artifacts in coronary imaging (122). While large challenges remain, the technical foundation needed to perform high-resolution MRI of human coronary atherosclerotic plaque *in vivo* is being steadily laid.

5.3 Strenghts and limitations

Our results must be interpreted under some limitations – primarily related to the *ex vivo* nature of the study. This setting offered ideal conditions for imaging of the coronary vessels with coronary CTA, especially with regard to motion artifacts. However coronary CT angiography can be performed with little to no motion artifacts using state of the art CT technology with improved temporal resolution and careful planning the exam (123,124). Although we injected a contrast agent into the coronary arteries, we presume that this did not reach the small neovessels within the plaques because we used a viscous contrast agent and a low pressure to push the contrast agent into the coronary

arteries. The second reason is that residual blood clots in the vasa vasorum prevent the contrast agent from entering the neovessels. In patients, the contrast agent will reach the neovessels during the first pass leading to an enhancement of the fibrous tissue around the necrotic core in advanced coronary atherosclerotic plaques. Thus, the number of plaques with a positive napkin-ring sign might be higher than in the present study. However Pflederer et al. reported a similar percentage of plaques with contrast-enhanced rims detected in culprit lesions in patients with ACS (44). For the present coronary CTA study, we used a scan protocol with a tube voltage of 120 kVp. While this has been the standard setting for many years, scan protocols using 100 kVp are now standard in smaller patients (125). The choice of scan protocol with lower kVp values alters the Hounsfield-units of all structures containing iodine and calcium, whereas the density values of other structures are not altered significantly (126). Thus, the selection of an imaging protocol of coronary CTA with 100 kVp might have slightly enhanced the detection of calcium. As the contrast material in the present study did not enter the plaque itself, the delineation of the necrotic core would not have been affected by such a protocol. Regarding the analysis of coronary CTA images several potential limitations merit consideration. Image sharpness was assessed subjectively, which introduced the possibility of bias into the study. Further, we did not evaluate potential radiation dose saving methods. Owing to increasing concern about the possible radiological–biological consequences of greater cumulative radiation doses from medical exposures, noise efficient reconstruction algorithms such as ASIR should be implemented to reduce radiation doses in cardiac CT protocols. Also the CNR relative to the pericoronary fat represents a surrogate measure of CT image quality that may not completely encompass all of the components needed to make a correct diagnosis. As such, it remains to be determined whether the increase in CNR achieved with MBIR and ASIR markedly increase coronary plaque evaluation. Furthermore, the computational algorithm for iterative image reconstruction algorithms varies between vendors and the use of MBIR is pre-commercial. In addition, iterative reconstruction algorithms are associated with increased reconstruction times due to their complex mathematical computation. However, this will be reduced with increasing computational capacity of the workstations and ASIR is already available as a real-time reconstruction algorithm (127). Although our study is to date the largest to investigate human coronaries with

MRI and coregistered histology, the procurement of broad range of human coronary artery specimens remains challenging. Certain plaque features such as hemorrhage and thrombus were thus not seen in our dataset. If present, however, the iron products in blood and fresh thrombus should be detected with our protocol by producing hyperintensity on the T1 and UTE images. The harvested coronary arteries were imaged with several modalities, and the nature of our study thus required tissue fixation to be performed. This, however, has been shown not to affect plaque assessment by MRI compared to unfixed specimens (112).

While these factors might limit the generality of our findings our approach offered the unique possibility to compare the CT morphology of advanced atherosclerotic plaques to the gold standard histopathology. Further research is needed to determine whether the study results can be translated into the clinical setting

DOI:10.14753/SE.2015.1797

6 Conclusions

Coronary atherosclerotic plaques with a napkin-ring sign in CT have a distinct histopathological appearance primarily characterized by a large necrotic core with a large fibrous component. Because these features have been associated with advanced atherosclerotic and rupture-prone lesions in histology, the napkin-ring sign can possibly serve as a marker for advanced lesions in coronary CT angiography.

Our initial results regarding image reconstruction of CT suggest that use of MBIR algorithm, as compared to ASIR and a standard FBPR reconstruction algorithm, leads to significantly improved image quality accompanied with a substantial decrease in image noise and increase of the CNR. These findings and the ability to achieve better vessel sharpness using MBIR compared to ASIR or FBPR may have an important clinical implication in the evaluation of the coronary artery tree that needs to be validated *in vivo*.

Applying automated plaque assessment in CT angiography, a significant portion of the automatically fitted vessel-wall boundaries must be corrected manually. The need for boundary correction is reproducible and shows a local relationship. However, MBIR leads to a significantly reduced need for correcting the automatically fitted boundaries compared to other reconstruction algorithms, especially at the site of calcifications. Thus, MBIR leads to a shorter assessment time and may improve the robustness of automated plaque assessment in coronary CTA.

Further, in our study we applied a novel combination of MRI contrast (T1, T2, and UTE) to image atherosclerotic plaque in human coronary arteries. We showed that plaque classification with this approach compares extremely favorably with histology. The addition of UTE MRI adds significant value by allowing plaque calcification to be accurately detected. Our study further underscores the potential of coronary plaque classification by MRI and its potential use to define the clinical stage of coronary atherosclerosis and guide patient management.

DOI:10.14753/SE.2015.1797

7 Summary

Cardiovascular disease related events remain the main cause of morbidity and mortality worldwide. Thus, there is a need of developing reliable non-invasive techniques potentiating early recognition of atherosclerotic disease. Coronary CT angiography has the potential to characterize atherosclerotic plaque beyond current clinical practice and discriminate vulnerable plaques from stable lesions. With the improvement of automated reading tools coronary CTA may also be used for large-scale clinical screening. The utility of MRI for assessing coronary atherosclerosis remains poorly described. Owing to its excellent soft tissue contrast MRI has the ability to accurately discriminate atherosclerotic plaque components. Still, accurate characterization of coronary atherosclerotic lesions must incorporate precise discrimination of calcified components, which limited by current MRI technique.

In our results we have defined the histopathological equivalent of the napkin-ring sing on CT, which has been understood as a marker of advanced coronary lesions. We showed, that the NRS is associated with large, advanced atherosclerotic lesion with a large necrotic core in histology. Our study also demonstrates that advanced CT image reconstruction techniques – such as MBIR – improve atherosclerotic plaque visualization. With further application of MBIR for automated plaque assessment, the necessary manual corrections of vessel-wall boundaries, thus the time for coronary segmentation and analysis is significantly decreased. Thus, the use of advanced image reconstruction algorithms, particularly MBIR improves the feasibility of automated plaque quantification and characterization. This may potentiate the spread of automated coronary CTA assessment tools in the daily clinical work and contribute to improved patients' management.

Furthermore, we demonstrated a novel approach with a combination T1, T2 and UTE MRI, that can accurately classify human coronary atherosclerotic lesions comprising lipid-rich and calcified plaques. Our MRI plaque classification scheme showed a strong correlation with histological data. These results underscore the potential of MRI for advanced atherosclerotic plaque characterization and its promising role in guidance of therapeutic interventions in patients with coronary artery disease.

DOI:10.14753/SE.2015.1797

8 Összefoglalás

A szív és érrendszeri betegségek vezetik a megbetegedési és halálozási statisztikákat világszerte. Ebből következően nagy igény áll fenn megbízható, a korai ateroszklerózis felismerését is lehetővé tevő nem invazív diagnosztikus eszközök fejlesztésére. A CT angiográfia vizsgálat alkalmas lehet a koronária ateroszklerotikus plakkok jelenlegi klinikai gyakorlaton túlmutató karakterizációjára, a potenciálisan vulnerábilis és stabil léziók elkülönítésére. Automatizált kiértékelő programok használatával a koronária CTA vizsgálat nagy szabású klinikai szűrésre is használható lehet. Az MR vizsgálat alkalmazhatósága koronária ateroszklerózis vizsgálatára kevésbé ismert. Kiváló kontraszt felbontásának köszönhetően azonban alkalmas lehet ateroszklerotikus plakk komponensek elkülönítésére. A koronária léziók pontos karakterizációja feltételezi a kalcifikált elemek elkülönítését is, mely a jelenleg használatos MR technikával kihívást jelent.

Munkámban meghatároztam a CT-n “napkin-ring” jelet mutató koronária plakkok szövettani jellegzetességeit, amely irodalmi adatok szerint nagy kockázatú plakk ismertető jegyének számít. Bizonyítottam, hogy a NRS szövettanilag előrehaladott, nagy méretű, nagy nekrotikus maggal rendelkező ateroszklerotikus plakknak feleltethető meg. Vizsgálatomban demonstráltam, hogy modern CT képrekonstrukciós technikák – mint az MBIR – javítják az ateroszklerotikus plakkok ábrázolását. Továbbá MBIR technika alkalmazásával automatikus plakk analízis szoftverek használata során lecsökken az érkontúr kijelölés manuális korrekciójának szükségessége, így a koronária szegmentációra és kép analízisre fordítandó idő. Ez összességében megbízhatóbb plakk kvantifikációt és karakterizációt tesz lehetővé, ami hozzájárulhat automatizált programok klinikai elterjedéséhez és a beteg menedzsment megkönnyítéséhez.

Munkám második részében egy új, T1, T2 és UTE szekvenciákból álló MRI technikát demonstráltam, mely humán koronária ateroszklerotikus plakkok, így lipiddús és kalcifikált léziók pontos osztályozását teszi lehetővé. Az alkalmazott plakk klasszifikációs séma erős korrelációt mutatott a szövettani osztályozással. Ezek az eredmények bíztatóan mutatnak rá az MR technika esetleges alkalmazhatóságára koronária betegek vizsgálata során.

DOI:10.14753/SE.2015.1797

9 References

1. Roger VL, Go AS, Lloyd-Jones DM, Adams RJ, Berry JD, Brown TM, Carnethon MR, Dai S, de Simone G, Ford ES, Fox CS, Fullerton HJ, Gillespie C, Greenlund KJ, Hailpern SM, Heit JA, Ho PM, Howard VJ, Kissela BM, Kittner SJ, Lackland DT, Lichtman JH, Lisabeth LD, Makuc DM, Marcus GM, Marelli A, Matchar DB, McDermott MM, Meigs JB, Moy CS, Mozaffarian D, Mussolino ME, Nichol G, Paynter NP, Rosamond WD, Sorlie PD, Stafford RS, Turan TN, Turner MB, Wong ND, Wylie-Rosett J, American Heart Association Statistics C, Stroke Statistics S. (2011) Heart disease and stroke statistics--2011 update: a report from the American Heart Association. Circulation, 123: e18-e209.
2. Naghavi M, Libby P, Falk E, Casscells SW, Litovsky S, Rumberger J, Badimon JJ, Stefanadis C, Moreno P, Pasterkamp G, Fayad Z, Stone PH, Waxman S, Raggi P, Madjid M, Zarrabi A, Burke A, Yuan C, Fitzgerald PJ, Siscovick DS, de Korte CL, Aikawa M, Juhani Airaksinen KE, Assmann G, Becker CR, Chesebro JH, Farb A, Galis ZS, Jackson C, Jang IK, Koenig W, Lodder RA, March K, Demirovic J, Navab M, Priori SG, Rekhter MD, Bahr R, Grundy SM, Mehran R, Colombo A, Boerwinkle E, Ballantyne C, Insull W, Jr., Schwartz RS, Vogel R, Serruys PW, Hansson GK, Faxon DP, Kaul S, Drexler H, Greenland P, Muller JE, Virmani R, Ridker PM, Zipes DP, Shah PK, Willerson JT. (2003) From vulnerable plaque to vulnerable patient: a call for new definitions and risk assessment strategies: Part I. Circulation, 108: 1664-72.
3. Falk E, Shah PK, Fuster V. (1995) Coronary plaque disruption. Circulation, 92: 657-71.
4. Stary HC, Chandler AB, Dinsmore RE, Fuster V, Glagov S, Insull W, Jr., Rosenfeld ME, Schwartz CJ, Wagner WD, Wissler RW. (1995) A definition of advanced types of atherosclerotic lesions and a histological classification of atherosclerosis. A report from the Committee on Vascular Lesions of the Council on Arteriosclerosis, American Heart Association. Circulation, 92: 1355-74.

5. Virmani R, Kolodgie FD, Burke AP, Farb A, Schwartz SM. (2000) Lessons from sudden coronary death: a comprehensive morphological classification scheme for atherosclerotic lesions. Arterioscler Thromb Vasc Biol, 20: 1262-75.
6. Virmani R, Burke AP, Farb A, Kolodgie FD. (2006) Pathology of the vulnerable plaque. J Am Coll Cardiol, 47: C13-8.
7. Kawasaki M, Bouma BE, Bressner J, Houser SL, Nadkarni SK, MacNeill BD, Jang IK, Fujiwara H, Tearney GJ. (2006) Diagnostic accuracy of optical coherence tomography and integrated backscatter intravascular ultrasound images for tissue characterization of human coronary plaques. J Am Coll Cardiol, 48: 81-8.
8. Jang IK, Tearney GJ, MacNeill B, Takano M, Moselewski F, Iftima N, Shishkov M, Houser S, Aretz HT, Halpern EF, Bouma BE. (2005) In vivo characterization of coronary atherosclerotic plaque by use of optical coherence tomography. Circulation, 111: 1551-5.
9. Bose D, von Birgelen C, Erbel R. (2007) Intravascular ultrasound for the evaluation of therapies targeting coronary atherosclerosis. J Am Coll Cardiol, 49: 925-32.
10. Nicholls SJ, Tuzcu EM, Sipahi I, Schoenhagen P, Nissen SE. (2006) Intravascular ultrasound in cardiovascular medicine. Circulation, 114: e55-9.
11. Yabushita H, Bouma BE, Houser SL, Aretz HT, Jang IK, Schlendorf KH, Kauffman CR, Shishkov M, Kang DH, Halpern EF, Tearney GJ. (2002) Characterization of human atherosclerosis by optical coherence tomography. Circulation, 106: 1640-5.
12. Libby P. (2013) Mechanisms of acute coronary syndromes and their implications for therapy. N Engl J Med, 368: 2004-13.
13. Arbab-Zadeh A, Nakano M, Virmani R, Fuster V. (2012) Acute coronary events. Circulation, 125: 1147-56.
14. Crea F, Liuzzo G. (2013) Pathogenesis of acute coronary syndromes. J Am Coll Cardiol, 61: 1-11.
15. Falk E, Nakano M, Bentzon JF, Finn AV, Virmani R. (2013) Update on acute coronary syndromes: the pathologists' view. Eur Heart J, 34: 719-28.
16. Stone GW, Maehara A, Lansky AJ, de Bruyne B, Cristea E, Mintz GS, Mehran

R, McPherson J, Farhat N, Marso SP, Parise H, Templin B, White R, Zhang Z, Serruys PW, Investigators P. (2011) A prospective natural-history study of coronary atherosclerosis. N Engl J Med, 364: 226-35.

17. Hoffmann U, Moselewski F, Nieman K, Jang IK, Ferencik M, Rahman AM, Cury RC, Abbara S, Joneidi-Jafari H, Achenbach S, Brady TJ. (2006) Noninvasive assessment of plaque morphology and composition in culprit and stable lesions in acute coronary syndrome and stable lesions in stable angina by multidetector computed tomography. J Am Coll Cardiol, 47: 1655-62.
18. Motoyama S, Sarai M, Harigaya H, Anno H, Inoue K, Hara T, Naruse H, Ishii J, Hishida H, Wong ND, Virmani R, Kondo T, Ozaki Y, Narula J. (2009) Computed tomographic angiography characteristics of atherosclerotic plaques subsequently resulting in acute coronary syndrome. J Am Coll Cardiol, 54: 49-57.
19. Schoenhagen P, Stone GW, Nissen SE, Grines CL, Griffin J, Clemson BS, Vince DG, Ziada K, Crowe T, Apperson-Hanson C, Kapadia SR, Tuzcu EM. (2003) Coronary plaque morphology and frequency of ulceration distant from culprit lesions in patients with unstable and stable presentation. Arterioscler Thromb Vasc Biol, 23: 1895-900.
20. Boden WE, O'Rourke RA, Teo KK, Hartigan PM, Maron DJ, Kostuk WJ, Knudtson M, Dada M, Casperson P, Harris CL, Chaitman BR, Shaw L, Gosselin G, Nawaz S, Title LM, Gau G, Blaustein AS, Booth DC, Bates ER, Spertus JA, Berman DS, Mancini GB, Weintraub WS, Group CTR. (2007) Optimal medical therapy with or without PCI for stable coronary disease. N Engl J Med, 356: 1503-16.
21. Finn AV, Nakano M, Narula J, Kolodgie FD, Virmani R. (2010) Concept of vulnerable/unstable plaque. Arterioscler Thromb Vasc Biol, 30: 1282-92.
22. Schaar JA, Muller JE, Falk E, Virmani R, Fuster V, Serruys PW, Colombo A, Stefanadis C, Ward Casscells S, Moreno PR, Maseri A, van der Steen AF. (2004) Terminology for high-risk and vulnerable coronary artery plaques. Report of a meeting on the vulnerable plaque, June 17 and 18, 2003, Santorini, Greece. Eur Heart J, 25: 1077-82.
23. Clarkson TB, Prichard RW, Morgan TM, Petrick GS, Klein KP. (1994)

Remodeling of coronary arteries in human and nonhuman primates. JAMA, 271: 289-94.

24. Yonetsu T, Kakuta T, Lee T, Takahashi K, Kawaguchi N, Yamamoto G, Koura K, Hishikari K, Iesaka Y, Fujiwara H, Isobe M. (2011) In vivo critical fibrous cap thickness for rupture-prone coronary plaques assessed by optical coherence tomography. Eur Heart J, 32: 1251-9.
25. Narula J, Nakano M, Virmani R, Kolodgie FD, Petersen R, Newcomb R, Malik S, Fuster V, Finn AV. (2013) Histopathologic characteristics of atherosclerotic coronary disease and implications of the findings for the invasive and noninvasive detection of vulnerable plaques. J Am Coll Cardiol, 61: 1041-51.
26. Maldonado N, Kelly-Arnold A, Vengrenyuk Y, Laudier D, Fallon JT, Virmani R, Cardoso L, Weinbaum S. (2012) A mechanistic analysis of the role of microcalcifications in atherosclerotic plaque stability: potential implications for plaque rupture. Am J Physiol Heart Circ Physiol, 303: H619-28.
27. Shah PK, Falk E, Badimon JJ, Fernandez-Ortiz A, Mailhac A, Villareal-Levy G, Fallon JT, Regnstrom J, Fuster V. (1995) Human monocyte-derived macrophages induce collagen breakdown in fibrous caps of atherosclerotic plaques. Potential role of matrix-degrading metalloproteinases and implications for plaque rupture. Circulation, 92: 1565-9.
28. Mach F, Schonbeck U, Bonnefoy JY, Pober JS, Libby P. (1997) Activation of monocyte/macrophage functions related to acute atheroma complication by ligation of CD40: induction of collagenase, stromelysin, and tissue factor. Circulation, 96: 396-9.
29. Libby P. (2008) The molecular mechanisms of the thrombotic complications of atherosclerosis. Journal of internal medicine, 263: 517-27.
30. Sugiyama S, Kugiyama K, Aikawa M, Nakamura S, Ogawa H, Libby P. (2004) Hypochlorous acid, a macrophage product, induces endothelial apoptosis and tissue factor expression: involvement of myeloperoxidase-mediated oxidant in plaque erosion and thrombogenesis. Arterioscler Thromb Vasc Biol, 24: 1309-14.
31. Davies MJ. (1996) The contribution of thrombosis to the clinical expression of coronary atherosclerosis. Thromb Res, 82: 1-32.

32. Arbustini E, Grasso M, Diegoli M, Pucci A, Bramerio M, Ardissino D, Angoli L, de Servi S, Bramucci E, Mussini A, et al. (1991) Coronary atherosclerotic plaques with and without thrombus in ischemic heart syndromes: a morphologic, immunohistochemical, and biochemical study. Am J Cardiol, 68: 36B-50B.
33. Davies MJ, Bland JM, Hangartner JR, Angelini A, Thomas AC. (1989) Factors influencing the presence or absence of acute coronary artery thrombi in sudden ischaemic death. Eur Heart J, 10: 203-8.
34. Cheruvu PK, Finn AV, Gardner C, Caplan J, Goldstein J, Stone GW, Virmani R, Muller JE. (2007) Frequency and distribution of thin-cap fibroatheroma and ruptured plaques in human coronary arteries: a pathologic study. J Am Coll Cardiol, 50: 940-9.
35. Hoffmann U, Ferencik M, Cury RC, Pena AJ. (2006) Coronary CT angiography. J Nucl Med, 47: 797-806.
36. Leber AW, Johnson T, Becker A, von Ziegler F, Tittus J, Nikolaou K, Reiser M, Steinbeck G, Becker CR, Knez A. (2007) Diagnostic accuracy of dual-source multi-slice CT-coronary angiography in patients with an intermediate pretest likelihood for coronary artery disease. Eur Heart J, 28: 2354-60.
37. Ferencik M, Chan RC, Achenbach S, Lisauskas JB, Houser SL, Hoffmann U, Abbara S, Cury RC, Bouma BE, Tearney GJ, Brady TJ. (2006) Arterial wall imaging: evaluation with 16-section multidetector CT in blood vessel phantoms and ex vivo coronary arteries. Radiology, 240: 708-16.
38. Leber AW, Knez A, von Ziegler F, Becker A, Nikolaou K, Paul S, Wintersperger B, Reiser M, Becker CR, Steinbeck G, Boekstegers P. (2005) Quantification of obstructive and nonobstructive coronary lesions by 64-slice computed tomography: a comparative study with quantitative coronary angiography and intravascular ultrasound. J Am Coll Cardiol, 46: 147-54.
39. Achenbach S, Moselewski F, Ropers D, Ferencik M, Hoffmann U, MacNeill B, Pohle K, Baum U, Anders K, Jang IK, Daniel WG, Brady TJ. (2004) Detection of calcified and noncalcified coronary atherosclerotic plaque by contrast-enhanced, submillimeter multidetector spiral computed tomography: a segment-based comparison with intravascular ultrasound. Circulation, 109: 14-7.
40. Knollmann F, Ducke F, Krist L, Kertesz T, Meyer R, Guski H, Felix R. (2008)

Quantification of atherosclerotic coronary plaque components by submillimeter computed tomography. Int J Cardiovasc Imaging, 24: 301-10.

41. Marwan M, Taher MA, El Meniawy K, Awadallah H, Pflederer T, Schuhback A, Ropers D, Daniel WG, Achenbach S. (2011) In vivo CT detection of lipid-rich coronary artery atherosclerotic plaques using quantitative histogram analysis: a head to head comparison with IVUS. Atherosclerosis, 215: 110-5.
42. Voros S, Rinehart S, Qian Z, Joshi P, Vazquez G, Fischer C, Belur P, Hulten E, Villines TC. (2011) Coronary atherosclerosis imaging by coronary CT angiography: current status, correlation with intravascular interrogation and meta-analysis. JACC Cardiovasc Imaging, 4: 537-48.
43. Kashiwagi M, Tanaka A, Kitabata H, Tsujioka H, Kataiwa H, Komukai K, Tanimoto T, Takemoto K, Takarada S, Kubo T, Hirata K, Nakamura N, Mizukoshi M, Imanishi T, Akasaka T. (2009) Feasibility of noninvasive assessment of thin-cap fibroatheroma by multidetector computed tomography. JACC Cardiovasc Imaging, 2: 1412-9.
44. Pflederer T, Marwan M, Schepis T, Ropers D, Seltmann M, Muschiol G, Daniel WG, Achenbach S. (2010) Characterization of culprit lesions in acute coronary syndromes using coronary dual-source CT angiography. Atherosclerosis, 211: 437-44.
45. Maurovich-Horvat P, Hoffmann U, Vorpahl M, Nakano M, Virmani R, Alkadhi H. (2010) The napkin-ring sign: CT signature of high-risk coronary plaques? JACC Cardiovasc Imaging, 3: 440-4.
46. Nishio M, Ueda Y, Matsuo K, Asai M, Nemoto T, Hirata A, Kashiwase K, Kodama K. (2011) Detection of disrupted plaques by coronary CT: comparison with angioscopy. Heart, 97: 1397-402.
47. Maurovich-Horvat P, Schlett CL, Alkadhi H, Nakano M, Otsuka F, Stolzmann P, Scheffel H, Ferencik M, Kriegel MF, Seifarth H, Virmani R, Hoffmann U. (2012) The Napkin-Ring Sign Indicates Advanced Atherosclerotic Lesions in Coronary CT Angiography. JACC Cardiovasc Imaging, 5: 1243-52.
48. Dey D, Schepis T, Marwan M, Slomka PJ, Berman DS, Achenbach S. (2010) Automated three-dimensional quantification of noncalcified coronary plaque from coronary CT angiography: comparison with intravascular US. Radiology,

257: 516-22.

49. Blackmon KN, Streck J, Thilo C, Bastarrika G, Costello P, Schoepf UJ. (2009) Reproducibility of automated noncalcified coronary artery plaque burden assessment at coronary CT angiography. J Thorac Imaging, 24: 96-102.
50. Marin D, Nelson RC, Schindera ST, Richard S, Youngblood RS, Yoshizumi TT, Samei E. (2010) Low-tube-voltage, high-tube-current multidetector abdominal CT: improved image quality and decreased radiation dose with adaptive statistical iterative reconstruction algorithm--initial clinical experience. Radiology, 254: 145-53.
51. Prakash P, Kalra MK, Ackman JB, Digumarthy SR, Hsieh J, Do S, Shepard JA, Gilman MD. (2010) Diffuse lung disease: CT of the chest with adaptive statistical iterative reconstruction technique. Radiology, 256: 261-9.
52. Yu Z, Thibault JB, Bouman CA, Sauer KD, Hsieh J. (2011) Fast model-based X-ray CT reconstruction using spatially nonhomogeneous ICD optimization. IEEE Trans Image Process, 20: 161-75.
53. Prakash P, Kalra MK, Kambadakone AK, Pien H, Hsieh J, Blake MA, Sahani DV. (2010) Reducing abdominal CT radiation dose with adaptive statistical iterative reconstruction technique. Invest Radiol, 45: 202-10.
54. Saam T, Hatsukami TS, Takaya N, Chu B, Underhill H, Kerwin WS, Cai J, Ferguson MS, Yuan C. (2007) The vulnerable, or high-risk, atherosclerotic plaque: noninvasive MR imaging for characterization and assessment. Radiology, 244: 64-77.
55. Saam T, Ferguson MS, Yarnykh VL, Takaya N, Xu D, Polissar NL, Hatsukami TS, Yuan C. (2005) Quantitative evaluation of carotid plaque composition by in vivo MRI. Arterioscler Thromb Vasc Biol, 25: 234-9.
56. Fabiano S, Mancino S, Stefanini M, Chiocchi M, Mauriello A, Spagnoli LG, Simonetti G. (2008) High-resolution multicontrast-weighted MR imaging from human carotid endarterectomy specimens to assess carotid plaque components. Eur Radiol, 18: 2912-21.
57. Yuan C, Mitsumori LM, Ferguson MS, Polissar NL, Echelard D, Ortiz G, Small R, Davies JW, Kerwin WS, Hatsukami TS. (2001) In vivo accuracy of multispectral magnetic resonance imaging for identifying lipid-rich necrotic

cores and intraplaque hemorrhage in advanced human carotid plaques. Circulation, 104: 2051-6.

58. Kerwin W, Hooker A, Spilker M, Vicini P, Ferguson M, Hatsukami T, Yuan C. (2003) Quantitative magnetic resonance imaging analysis of neovasculature volume in carotid atherosclerotic plaque. Circulation, 107: 851-6.
59. Hatsukami TS, Ross R, Polissar NL, Yuan C. (2000) Visualization of fibrous cap thickness and rupture in human atherosclerotic carotid plaque in vivo with high-resolution magnetic resonance imaging. Circulation, 102: 959-64.
60. Chan CF, Keenan NG, Nielles-Vallespin S, Gatehouse P, Sheppard MN, Boyle JJ, Pennell DJ, Firmin DN. (2010) Ultra-short echo time cardiovascular magnetic resonance of atherosclerotic carotid plaque. J Cardiovasc Magn Reson, 12: 17.
61. Sharma S, Boujraf S, Bornstedt A, Hombach V, Ignatius A, Oberhuber A, Rasche V. (2010) Quantification of calcifications in endarterectomy samples by means of high-resolution ultra-short echo time imaging. Invest Radiol, 45: 109-13.
62. van Elderen SGC, Versluis MJ, Westenberg JJM, Agarwal H, Smith NB, Stuber M, de Roos A, Webb AG. (2010) Right Coronary MR Angiography at 7 T: A Direct Quantitative and Qualitative Comparison with 3 T in Young Healthy Volunteers. Radiology, 257: 254-259.
63. Snyder CJ, DelaBarre L, Metzger GJ, van de Moortele PF, Akgun C, Ugurbil K, Vaughan JT. (2009) Initial results of cardiac imaging at 7 Tesla. Magn Reson Med, 61: 517-24.
64. Vaughan JT, Snyder CJ, DelaBarre LJ, Bolan PJ, Tian J, Bolinger L, Adriany G, Andersen P, Strupp J, Ugurbil K. (2009) Whole-body imaging at 7T: preliminary results. Magn Reson Med, 61: 244-8.
65. Versluis MJ, Tsekos N, Smith NB, Webb AG. (2009) Simple RF design for human functional and morphological cardiac imaging at 7tesla. J Magn Reson, 200: 161-6.
66. Frauenrath T, Hezel F, Heinrichs U, Kozerke S, Utting JF, Kob M, Butenweg C, Boesiger P, Niendorf T. (2009) Feasibility of cardiac gating free of interference with electro-magnetic fields at 1.5 Tesla, 3.0 Tesla and 7.0 Tesla using an MR-

stethoscope. Invest Radiol, 44: 539-47.

67. van Elderen SG, Versluis MJ, Webb AG, Westenberg JJ, Doornbos J, Smith NB, de Roos A, Stuber M. (2009) Initial results on in vivo human coronary MR angiography at 7 T. Magn Reson Med, 62: 1379-84.
68. Itskovich VV, Samber DD, Mani V, Aguinaldo JG, Fallon JT, Tang CY, Fuster V, Fayad ZA. (2004) Quantification of human atherosclerotic plaques using spatially enhanced cluster analysis of multicontrast-weighted magnetic resonance images. Magn Reson Med, 52: 515-23.
69. Maurovich-Horvat P, Schlett CL, Alkadhi H, Nakano M, Stolzmann P, Vorpahl M, Scheffel H, Tanaka A, Warger WC, 2nd, Maehara A, Ma S, Kriegel MF, Kaple RK, Seifarth H, Bamberg F, Mintz GS, Tearney GJ, Virmani R, Hoffmann U. (2012) Differentiation of Early from Advanced Coronary Atherosclerotic Lesions: Systematic Comparison of CT, Intravascular US, and Optical Frequency Domain Imaging with Histopathologic Examination in ex Vivo Human Hearts. Radiology, 265: 393-401.
70. Flohr TG, Schaller S, Stierstorfer K, Bruder H, Ohnesorge BM, Schoepf UJ. (2005) Multi-detector row CT systems and image-reconstruction techniques. Radiology, 235: 756-73.
71. Beister M, Kolditz D, Kalender WA. (2012) Iterative reconstruction methods in X-ray CT. Phys Med, 28: 94-108.
72. Katsura M, Matsuda I, Akahane M, Sato J, Akai H, Yasaka K, Kunimatsu A, Ohtomo K. (2012) Model-based iterative reconstruction technique for radiation dose reduction in chest CT: comparison with the adaptive statistical iterative reconstruction technique. Eur Radiol, 22: 1613-23.
73. Thibault JB, Sauer KD, Bouman CA, Hsieh J. (2007) A three-dimensional statistical approach to improved image quality for multislice helical CT. Med Phys, 34: 4526-44.
74. Kolodgie FD, Gold HK, Burke AP, Fowler DR, Kruth HS, Weber DK, Farb A, Guerrero LJ, Hayase M, Kutys R, Narula J, Finn AV, Virmani R. (2003) Intraplaque hemorrhage and progression of coronary atheroma. N Engl J Med, 349: 2316-25.
75. Burke AP KF, Virmani R. . Pathogenesis and significance of calcification in

coronary atherosclerosis. In: Virmani R, Narula J, Leon MB, editors. The vulnerable atherosclerotic plaque: strategies for diagnosis and management.: Malden: Wiley-Blackwell; p. 77-94., 2006.

76. Araoz PA, Kirsch J, Primak AN, Braun NN, Saba O, Williamson EE, Harmsen WS, Mandrekar JN, McCollough CH. (2009) Optimal image reconstruction phase at low and high heart rates in dual-source CT coronary angiography. Int J Cardiovasc Imaging, 25: 837-45.
77. Weustink AC, Mollet NR, Pugliese F, Meijboom WB, Nieman K, Heijenbrok-Kal MH, Flohr TG, Neefjes LA, Cademartiri F, de Feyter PJ, Krestin GP. (2008) Optimal electrocardiographic pulsing windows and heart rate: effect on image quality and radiation exposure at dual-source coronary CT angiography. Radiology, 248: 792-8.
78. Boogers MJ, Broersen A, van Velzen JE, de Graaf FR, El-Naggar HM, Kitslaar PH, Dijkstra J, Delgado V, Boersma E, de Roos A, Schuijf JD, Schalij MJ, Reiber JH, Bax JJ, Jukema JW. (2012) Automated quantification of coronary plaque with computed tomography: comparison with intravascular ultrasound using a dedicated registration algorithm for fusion-based quantification. Eur Heart J, 33: 1007-16.
79. Cai JM, Hatsukami TS, Ferguson MS, Small R, Polissar NL, Yuan C. (2002) Classification of human carotid atherosclerotic lesions with in vivo multicontrast magnetic resonance imaging. Circulation, 106: 1368-73.
80. Landis JR, Koch GG. (1977) The measurement of observer agreement for categorical data. Biometrics, 33: 159-74.
81. Watanabe Y, Nakazawa T, Higashi M, Itoh T, Naito H. (2011) Assessment of calcified carotid plaque volume: comparison of contrast-enhanced dual-energy CT angiography and native single-energy CT. AJR Am J Roentgenol, 196: W796-9.
82. Siegel S CN. Nonparametric Statistics for the Behavioral Sciences. International Edition ed: McGraw-Hill Book Company New York, 1988.
83. Motoyama S, Kondo T, Anno H, Sugiura A, Ito Y, Mori K, Ishii J, Sato T, Inoue K, Sarai M, Hishida H, Narula J. (2007) Atherosclerotic plaque characterization by 0.5-mm-slice multislice computed tomographic imaging. Circ J, 71: 363-6.

84. Motoyama S, Kondo T, Sarai M, Sugiura A, Harigaya H, Sato T, Inoue K, Okumura M, Ishii J, Anno H, Virmani R, Ozaki Y, Hishida H, Narula J. (2007) Multislice computed tomographic characteristics of coronary lesions in acute coronary syndromes. J Am Coll Cardiol, 50: 319-26.

85. Pohle K, Achenbach S, Macneill B, Ropers D, Ferencik M, Moselewski F, Hoffmann U, Brady TJ, Jang IK, Daniel WG. (2007) Characterization of non-calcified coronary atherosclerotic plaque by multi-detector row CT: comparison to IVUS. Atherosclerosis, 190: 174-80.

86. Ino Y, Kubo T, Tanaka A, Kuroi A, Tsujioka H, Ikejima H, Okouchi K, Kashiwagi M, Takarada S, Kitabata H, Tanimoto T, Komukai K, Ishibashi K, Kimura K, Hirata K, Mizukoshi M, Imanishi T, Akasaka T. (2011) Difference of culprit lesion morphologies between ST-segment elevation myocardial infarction and non-ST-segment elevation acute coronary syndrome: an optical coherence tomography study. JACC Cardiovasc Interv, 4: 76-82.

87. Stary HC, Chandler AB, Glagov S, Guyton JR, Insull W, Jr., Rosenfeld ME, Schaffer SA, Schwartz CJ, Wagner WD, Wissler RW. (1994) A definition of initial, fatty streak, and intermediate lesions of atherosclerosis. A report from the Committee on Vascular Lesions of the Council on Arteriosclerosis, American Heart Association. Circulation, 89: 2462-78.

88. Burke AP, Virmani R, Galis Z, Haudenschild CC, Muller JE. (2003) 34th Bethesda Conference: Task force #2--What is the pathologic basis for new atherosclerosis imaging techniques? J Am Coll Cardiol, 41: 1874-86.

89. Gossl M, Versari D, Hildebrandt HA, Bajanowski T, Sangiorgi G, Erbel R, Ritman EL, Lerman LO, Lerman A. (2010) Segmental heterogeneity of vasa vasorum neovascularization in human coronary atherosclerosis. JACC Cardiovasc Imaging, 3: 32-40.

90. Virmani R, Kolodgie FD, Burke AP, Finn AV, Gold HK, Tulenko TN, Wrenn SP, Narula J. (2005) Atherosclerotic plaque progression and vulnerability to rupture: angiogenesis as a source of intraplaque hemorrhage. Arterioscler Thromb Vasc Biol, 25: 2054-61.

91. Aikawa E, Nahrendorf M, Figueiredo JL, Swirski FK, Shtatland T, Kohler RH, Jaffer FA, Aikawa M, Weissleder R. (2007) Osteogenesis associates with

inflammation in early-stage atherosclerosis evaluated by molecular imaging in vivo. Circulation, 116: 2841-50.

92. Yanagawa M, Honda O, Yoshida S, Kikuyama A, Inoue A, Sumikawa H, Koyama M, Tomiyama N. (2010) Adaptive statistical iterative reconstruction technique for pulmonary CT: image quality of the cadaveric lung on standard- and reduced-dose CT. Acad Radiol, 17: 1259-66.
93. Ziegler A, Kohler T, Proksa R. (2007) Noise and resolution in images reconstructed with FBP and OSC algorithms for CT. Med Phys, 34: 585-98.
94. Prakash P, Kalra MK, Digumarthy SR, Hsieh J, Pien H, Singh S, Gilman MD, Shepard JA. (2010) Radiation dose reduction with chest computed tomography using adaptive statistical iterative reconstruction technique: initial experience. J Comput Assist Tomogr, 34: 40-5.
95. Fuchs TA, Fiechter M, Gebhard C, Stehli J, Ghadri JR, Kazakauskaite E, Herzog BA, Husmann L, Gaemperli O, Kaufmann PA. (2013) CT coronary angiography: impact of adapted statistical iterative reconstruction (ASIR) on coronary stenosis and plaque composition analysis. Int J Cardiovasc Imaging, 29: 719-24.
96. Hou Y, Liu X, Xv S, Guo W, Guo Q. (2012) Comparisons of image quality and radiation dose between iterative reconstruction and filtered back projection reconstruction algorithms in 256-MDCT coronary angiography. AJR Am J Roentgenol, 199: 588-94.
97. Yoo RE, Park EA, Lee W, Shim H, Kim YK, Chung JW, Park JH. (2013) Image quality of adaptive iterative dose reduction 3D of coronary CT angiography of 640-slice CT: comparison with filtered back-projection. Int J Cardiovasc Imaging, 29: 669-76.
98. Schuhbaeck A, Achenbach S, Layritz C, Eisentopf J, Hecker F, Pflederer T, Gauss S, Rixe J, Kalender W, Daniel WG, Lell M, Ropers D. (2012) Image quality of ultra-low radiation exposure coronary CT angiography with an effective dose <0.1 mSv using high-pitch spiral acquisition and raw data-based iterative reconstruction. Eur Radiol.
99. Moscariello A, Takx RA, Schoepf UJ, Renker M, Zwerner PL, O'Brien TX, Allmendinger T, Vogt S, Schmidt B, Savino G, Fink C, Bonomo L, Henzler T.

(2011) Coronary CT angiography: image quality, diagnostic accuracy, and potential for radiation dose reduction using a novel iterative image reconstruction technique-comparison with traditional filtered back projection. Eur Radiol, 21: 2130-8.

100. Voros S, Rinehart S, Qian Z, Vazquez G, Anderson H, Murrieta L, Wilmer C, Carlson H, Taylor K, Ballard W, Karmpaliotis D, Kalynych A, Brown C, 3rd. (2011) Prospective validation of standardized, 3-dimensional, quantitative coronary computed tomographic plaque measurements using radiofrequency backscatter intravascular ultrasound as reference standard in intermediate coronary arterial lesions: results from the ATLANTA (assessment of tissue characteristics, lesion morphology, and hemodynamics by angiography with fractional flow reserve, intravascular ultrasound and virtual histology, and noninvasive computed tomography in atherosclerotic plaques) I study. JACC Cardiovasc Interv, 4: 198-208.
101. Renker M, Nance JW, Jr., Schoepf UJ, O'Brien TX, Zwerner PL, Meyer M, Kerl JM, Bauer RW, Fink C, Vogl TJ, Henzler T. (2011) Evaluation of heavily calcified vessels with coronary CT angiography: comparison of iterative and filtered back projection image reconstruction. Radiology, 260: 390-9.
102. Ebersberger U, Tricarico F, Schoepf UJ, Blanke P, Spears JR, Rowe GW, Halligan WT, Henzler T, Bamberg F, Leber AW, Hoffmann E, Apfaltrer P. (2013) CT evaluation of coronary artery stents with iterative image reconstruction: improvements in image quality and potential for radiation dose reduction. Eur Radiol, 23: 125-32.
103. Funama Y, Oda S, Utsunomiya D, Taguchi K, Shimonobo T, Yamashita Y, Awai K. (2012) Coronary artery stent evaluation by combining iterative reconstruction and high-resolution kernel at coronary CT angiography. Acad Radiol, 19: 1324-31.
104. Stolzmann P, Schlett CL, Maurovich-Horvat P, Maehara A, Ma S, Scheffel H, Engel LC, Karolyi M, Mintz GS, Hoffmann U. (2012) Variability and accuracy of coronary CT angiography including use of iterative reconstruction algorithms for plaque burden assessment as compared with intravascular ultrasound-an ex vivo study. Eur Radiol, 22: 2067-75.

105. Nance JW, Jr., Schlett CL, Schoepf UJ, Oberoi S, Leisy HB, Barraza JM, Jr., Headden GF, Nikolaou K, Bamberg F. (2012) Incremental prognostic value of different components of coronary atherosclerotic plaque at cardiac CT angiography beyond coronary calcification in patients with acute chest pain. Radiology, 264: 679-90.

106. Ferencik M, Schlett CL, Ghoshhajra BB, Kriegel MF, Joshi SB, Maurovich-Horvat P, Rogers IS, Banerji D, Bamberg F, Truong QA, Brady TJ, Nagurney JT, Hoffmann U. (2012) A computed tomography-based coronary lesion score to predict acute coronary syndrome among patients with acute chest pain and significant coronary stenosis on coronary computed tomographic angiogram. Am J Cardiol, 110: 183-9.

107. Cheng GC, Loree HM, Kamm RD, Fishbein MC, Lee RT. (1993) Distribution of circumferential stress in ruptured and stable atherosclerotic lesions. A structural analysis with histopathological correlation. Circulation, 87: 1179-87.

108. Huang H, Virmani R, Younis H, Burke AP, Kamm RD, Lee RT. (2001) The impact of calcification on the biomechanical stability of atherosclerotic plaques. Circulation, 103: 1051-6.

109. Mintz GS, Pichard AD, Popma JJ, Kent KM, Satler LF, Bucher TA, Leon MB. (1997) Determinants and correlates of target lesion calcium in coronary artery disease: a clinical, angiographic and intravascular ultrasound study. J Am Coll Cardiol, 29: 268-74.

110. Taylor AJ, Burke AP, O'Malley PG, Farb A, Malcom GT, Smialek J, Virmani R. (2000) A comparison of the Framingham risk index, coronary artery calcification, and culprit plaque morphology in sudden cardiac death. Circulation, 101: 1243-8.

111. Cai J, Hatsukami TS, Ferguson MS, Kerwin WS, Saam T, Chu B, Takaya N, Polissar NL, Yuan C. (2005) In vivo quantitative measurement of intact fibrous cap and lipid-rich necrotic core size in atherosclerotic carotid plaque: comparison of high-resolution, contrast-enhanced magnetic resonance imaging and histology. Circulation, 112: 3437-44.

112. Sun B, Giddens DP, Long R, Jr., Taylor WR, Weiss D, Joseph G, Vega D, Oshinski JN. (2006) Characterization of coronary atherosclerotic plaque using

multicontrast MRI acquired under simulated in vivo conditions. J Magn Reson Imaging, 24: 833-41.

113. Oei ML, Ozgun M, Seifarth H, Bunck A, Fischbach R, Orwat S, Heindel W, Botnar R, Maintz D. (2010) T1-weighted MRI for the detection of coronary artery plaque haemorrhage. Eur Radiol, 20: 2817-23.
114. Mani V, Briley-Saebo KC, Itskovich VV, Samber DD, Fayad ZA. (2006) Gradient echo acquisition for superparamagnetic particles with positive contrast (GRASP): sequence characterization in membrane and glass superparamagnetic iron oxide phantoms at 1.5T and 3T. Magn Reson Med, 55: 126-35.
115. Chu B, Kampschulte A, Ferguson MS, Kerwin WS, Yarnykh VL, O'Brien KD, Polissar NL, Hatsukami TS, Yuan C. (2004) Hemorrhage in the atherosclerotic carotid plaque: a high-resolution MRI study. Stroke, 35: 1079-84.
116. Moody AR, Murphy RE, Morgan PS, Martel AL, Delay GS, Allder S, MacSweeney ST, Tennant WG, Gladman J, Lowe J, Hunt BJ. (2003) Characterization of complicated carotid plaque with magnetic resonance direct thrombus imaging in patients with cerebral ischemia. Circulation, 107: 3047-52.
117. Reichert IL, Robson MD, Gatehouse PD, He T, Chappell KE, Holmes J, Girgis S, Bydder GM. (2005) Magnetic resonance imaging of cortical bone with ultrashort TE pulse sequences. Magn Reson Imaging, 23: 611-8.
118. Fayad ZA, Fuster V, Fallon JT, Jayasundera T, Worthley SG, Helft G, Aguinaldo JG, Badimon JJ, Sharma SK. (2000) Noninvasive in vivo human coronary artery lumen and wall imaging using black-blood magnetic resonance imaging. Circulation, 102: 506-10.
119. Yeon SB, Sabir A, Clouse M, Martinezclark PO, Peters DC, Hauser TH, Gibson CM, Nezafat R, Maintz D, Manning WJ, Botnar RM. (2007) Delayed-enhancement cardiovascular magnetic resonance coronary artery wall imaging: comparison with multislice computed tomography and quantitative coronary angiography. J Am Coll Cardiol, 50: 441-7.
120. Chu B, Phan BA, Balu N, Yuan C, Brown BG, Zhao XQ. (2006) Reproducibility of carotid atherosclerotic lesion type characterization using high resolution multicontrast weighted cardiovascular magnetic resonance. J Cardiovasc Magn Reson, 8: 793-9.

121. Grassl A, Winter L, Thalhammer C, Renz W, Kellman P, Martin C, von Knobelsdorff-Brenkenhoff F, Tkachenko V, Schulz-Menger J, Niendorf T. (2011) Design, evaluation and application of an eight channel transmit/receive coil array for cardiac MRI at 7.0T. Eur J Radiol.

122. Schmitt M, Potthast A, Sosnovik DE, Polimeni JR, Wiggins GC, Triantafyllou C, Wald LL. (2008) A 128-channel receive-only cardiac coil for highly accelerated cardiac MRI at 3 Tesla. Magn Reson Med, 59: 1431-9.

123. Dewey M, Vavere AL, Arbab-Zadeh A, Miller JM, Sara L, Cox C, Gottlieb I, Yoshioka K, Paul N, Hoe J, de Roos A, Lardo AC, Lima JA, Clouse ME. (2010) Patient characteristics as predictors of image quality and diagnostic accuracy of MDCT compared with conventional coronary angiography for detecting coronary artery stenoses: CORE-64 Multicenter International Trial. AJR Am J Roentgenol, 194: 93-102.

124. Seifarth H, Wienbeck S, Pusken M, Juergens KU, Maintz D, Vahlhaus C, Heindel W, Fischbach R. (2007) Optimal systolic and diastolic reconstruction windows for coronary CT angiography using dual-source CT. AJR Am J Roentgenol, 189: 1317-23.

125. Scheffel H, Alkadhi H, Leschka S, Plass A, Desbiolles L, Guber I, Krauss T, Gruenenfelder J, Genoni M, Luescher TF, Marincek B, Stolzmann P. (2008) Low-dose CT coronary angiography in the step-and-shoot mode: diagnostic performance. Heart, 94: 1132-7.

126. Barreto M, Schoenhagen P, Nair A, Amatangelo S, Milite M, Obuchowski NA, Lieber ML, Halliburton SS. (2008) Potential of dual-energy computed tomography to characterize atherosclerotic plaque: ex vivo assessment of human coronary arteries in comparison to histology. J Cardiovasc Comput Tomogr, 2: 234-42.

127. Nelson RC, Feuerlein S, Boll DT. (2011) New iterative reconstruction techniques for cardiovascular computed tomography: how do they work, and what are the advantages and disadvantages? J Cardiovasc Comput Tomogr, 5: 286-92.

DOI:10.14753/SE.2015.1797

10 Publications

10.1 Publications closely related to the present thesis

1. **Károlyi M**, Seifarth H, Liew GY, Schlett CL, Maurovich-Horvat P, Stolzmann P, Dai G, Huang S, Georgen CJ, Nakano M, Otsuka F, Virmani R, Hoffmann U, Sosnovik DE. (2013) Classification of Coronary Atherosclerotic Plaques Ex Vivo with T1, T2 and Ultrashort Echo Time CMR. JACC Cardiovasc Imaging, 6: 466-74. **IF: 6.986**
2. Seifarth H, Schlett CL, Nakano M, Otsuka F, **Károlyi M**, Liew G, Maurovich-Horvat P, Alkadhi H, Virmani R, Hoffmann U. (2012) Histopathological correlates of the napkin-ring sign plaque in coronary CT angiography. Atherosclerosis, 224: 90-6. **IF: 3.706**
3. Scheffel H, Stolzmann P, Schlett CL, Engel LC, Major GP, **Károlyi M**, Do S, Maurovich-Horvat P, Hoffmann U. (2012) Coronary atherosclerotic plaques: Cardiac CT with model-based and adaptive-statistical iterative reconstruction technique. Eur J Radiol, 81: 363-9. **IF: 2.512**
4. Puchner SB, Ferencik M, **Károlyi M**, Do S, Maurovich-Horvat P, Kauczor HU, Hoffmann U, Schlett CL. (2013) The Effect of Iterative Image Reconstruction Algorithms on the Feasibility of Automated Plaque Assessment in Coronary CT Angiography. Int J Cardiovasc Imaging. 29: 1879-8. **IF: 2.322**

10.2 Publications not related to the present thesis

Original articles

1. Stolzmann P, Schlett CL, Maurovich-Horvat P, Maehara A, Ma S, Scheffel H, Engel LC, **Károlyi M**, Mintz GS, Hoffmann U. (2012) Variability and accuracy of coronary CT angiography including use of iterative reconstruction algorithms for plaque burden assessment as compared with intravascular ultrasound-an ex vivo study. Eur Radiol, 22: 2067-75. **IF: 3.548**

2. Ghoshhajra BB, Engel LC, **Károlyi M**, Sidhu MS, Wai B, Barreto M, Shanmugam U, Hoffmann U, Brady TJ, Kalra M, Abbara S. (2013) Cardiac computed tomography with automatic tube potential selection. Effects on radiation dose and image quality. J Thorac Imaging, 28: 40-8. **IF: 1.489**
3. Ghoshhajra BB, Engel LC, Major GP, Verdini D, Sidhu M, **Károlyi M**, Abbara S, Hoffmann U, Karla M, Brady TJ. (2011) Direct chest area measurement: A potential anthropometric replacement for BMI to inform cardiac CT dose parameters? J Cardiovasc Comput Tomogr; 5: 240-6 **IF: N/A**
4. Engel LC, Ferencik M, Liew GY, **Karolyi M**, Sidhu MS, Lee AM, Wai B, Blankstein R, Abbara S, Hoffmann U, Ghoshhajra BB. (2012) Ultra-Low Dose Cardiac CT Angiography at 80 kV using Second Generation Dual-Source CT: Assessment of Radiation Dose and Image Quality. J Med Diag Met, 1:1 **IF: N/A**

Review articles

1. Bartykowszki A, Celeng Cs, **Karolyi M**, Maurovich-Horvat P. (2014) High Risk Features on Coronary CT Angiography. Curr Cardiovasc Imaging Rep, 7: 9279.

Articles in Hungarian

1. Maurovich-Horvat P, Bartykowszki A, Kerecsen G, Thury A, **Károlyi M**, Balázs Gy, Várady E, Tóth L, Pintér N, Szukits S, Kolozsvári R, Hoffer K, Király I, Nagy L, Hüttl K, Préda I, Palkó A, Kiss Róbert G, Battyány I, Merkely B. (2013) A koronária CT-angiográfia leletezése. A Magyar Kardiológusok Társasága Szív-CT Munkacsoportjának és a Magyar Radiológusok Társasága Szív Képalkotó Diagnosztikai Szekciójának közös ajánlása. Cardiologica Hungarica, 43: 275-281.

DOI:10.14753/SE.2015.1797

11 Acknowledgements

First and foremost, I would like to dedicate my dissertation to the loving memory of my mother. She was my greatest mentor, whose belief, fortitude and never resting encouragement motivated me all along my career.

I would like to express my greatest gratitude to Dr. Pál Maurovich-Horvat, my PhD supervisor and tutor in the past three years. His dedication to research inspired me throughout my doctoral work. Dr. Maurovich-Horvat's guidance was highly instrumental to set up my research work in Boston and learn the clinical aspects of cardiac CT in Budapest. His constant help, friendly manner, all time availability and encouragement were a great help for me all along the way to the doctoral thesis.

Furthermore, I would like to gratefully thank Professor Béla Merkely for his generous support during my early carrier. Professor Merkely has directed my interest to cardiovascular medicine and mentored me throughout the student and doctoral years. I am very thankful to him for supporting me to participate in the Professional Internship Program of the Hungarian American Enterprise Scholarship Fund, which enabled me to exchange knowledge and expertise with the Cardiac MR PET CT Program in the Massachusetts General Hospital, Harvard Medical School.

I would like to gratefully thank the support of Professor Udo Hoffmann who allowed me to join his research group in Boston and helped me with the analysis and interpretation of the data. I also thank Professor David E. Sosnovik for sharing his expertise on cardiac magnetic resonance and for his helpful discussion on the manuscript that is the subject of the present thesis. Furthermore, I would like to thank to all my colleagues at the Cardiac MR PET CT Program, especially to Dr. Cristopher L. Schlett, Dr. Paul Stolzmann, Dr. Brian B. Ghoshhajra, Dr. Hans Scheffel, Dr. Harald Seifarth, Dr. Leif C. Engel, Dr. Stefan B. Puchner and Dr. Alexander Goehler for their contribution to my research in Boston. It was a pleasure to work in this inspiring environment.

Last, but not least I am thankful to all my colleagues and friends at the Heart and Vascular Center of Semmelweis University, who supported my research with valuable discussions and contributed to a great atmosphere of all day work.

DOI:10.14753/SE.2015.1797

Appendix (Paper 1-4)